

LhARA: The Laser-hybrid Accelerator for Radiobiological Applications

G. Aymar¹, T. Becker², S. Boogert³, M. Borghesi⁴, R. Bingham^{5,1},
C. Brenner¹, P.N. Burrows⁶, O.C. Ettliger⁷, T. Dascalu⁸, S. Gibson³,
T. Greenshaw⁹, S. Gruber¹⁰, D. Gujral¹¹, C. Hardiman¹¹, J. Hughes⁹,
W.G. Jones^{8,20}, K. Kirkby¹², A. Kurup⁸, J-B. Lagrange¹, K. Long^{8,1}, W. Luk⁸,
J. Matheson¹, P. McKenna^{5,14}, R. Mclauchlan¹¹, Z. Najmudin⁷, H.T. Lau⁸,
J.L. Parsons^{9,21}, J. Pasternak^{8,1}, J. Pozimski^{8,1}, K. Prise⁴, M. Puchalska¹³,
P. Ratoff¹⁴, G. Schettino^{15,19}, W. Shields³, S. Smith¹⁶, J. Thomason¹,
S. Towe¹⁷, P. Weightman⁸, C. Whyte⁵, R. Xiao¹⁸

¹ STFC Rutherford Appleton Laboratory, Harwell Oxford, Didcot, OX11 0QX, UK

² Maxeler Technologies Limited, 3 Hammersmith Grove, London W6 0ND, UK

³ John Adams Institute for Accelerator Science, Royal Holloway, University of London, Egham, Surrey, TW20 0EX, UK

⁴ Queens University Belfast, University Road, Belfast, BT7 1NN, Northern Ireland, UK

⁵ Department of Physics, SUPA, University of Strathclyde, 16 Richmond Street, Glasgow, G1 1XQ, UK

⁶ John Adams Institute for Accelerator Science, University of Oxford, Denys Wilkinson Building, Keble Road, Oxford OX1 3RH, UK

⁷ John Adams Institute for Accelerator Science, Imperial College London, Exhibition Road, London, SW7 2AZ, UK

⁸ Imperial College London, Exhibition Road, London, SW7 2AZ, UK

⁹ University of Liverpool, Liverpool L3 9TA, UK

¹⁰ Christian Doppler Laboratory for Medical Radiation Research for Radiation Oncology, Medical University of Vienna, Spitalgasse 23, 1090 Vienna, Austria

¹¹ Imperial College NHS Healthcare Trust, The Bays, South Wharf Road, St Mary's Hospital, London W2 1NY, UK

¹² University of Manchester, Oxford Road, Manchester, M13 9PL, UK

¹³ Technische Universität Wien, Atominstytut, Stadionallee 2, 1020 Vienna, Austria

¹⁴ Cockcroft Institute, Daresbury Laboratory, Sci-Tech Daresbury, Daresbury, Warrington, WA4 4AD, UK

¹⁵ National Physical Laboratory, Hampton Road, Teddington, Middlesex, TW11 0LW, UK

¹⁶ STFC Daresbury Laboratory, Daresbury, Cheshire, WA4 4AD, UK

¹⁷ Leo Cancer Care, Broadview, Windmill Hill, Hailsham, East Sussex, BN27 4RY, UK

¹⁸ Corerain Technologies, 14F, Changfu Jinmao Building (CFC), Trade-free Zone, Futian District, Shenzhen, Guangdong, China

¹⁹ University of Surrey, 388 Stag Hill, Guilford, GU2 7XH, UK

²⁰ Imperial Patient and Public Involvement Group (IPPIG), Imperial College London, Exhibition Road, London, SW7 2AZ, UK

²¹ The Clatterbridge Cancer Centre, Bebington, CH63 4JY, UK

This is a provisional file, not the final typeset article

Correspondence:

A. Kurup

a.kurup@imperial.ac.uk

2 ABSTRACT

3 The 'Laser-hybrid Accelerator for Radiobiological Applications', LhARA, is conceived as a novel,
4 flexible facility dedicated to the study of radiobiology. The technologies demonstrated in LhARA,
5 which have wide application, will be developed to allow particle-beam therapy to be delivered in
6 a new regimen, combining a variety of ion species in a single treatment fraction and exploiting
7 ultra-high dose rates. LhARA will be a hybrid accelerator system in which laser interactions drive
8 the creation of a large flux of protons or light ions that are captured using a plasma (Gabor)
9 lens and formed into a beam. The laser-driven source allows protons and ions to be captured
10 at energies significantly above those that pertain in conventional facilities, thus evading the
11 current space-charge limit on the instantaneous dose rate that can be delivered. The laser-hybrid
12 approach, therefore, will allow the radiobiology that determines the response of tissue to ionising
13 radiation to be studied with protons and light ions using a wide variety of time structures, spectral
14 distributions, and spatial configurations at instantaneous dose rates up to and significantly beyond
15 the ultra-high dose-rate 'FLASH' regime.

16 It is proposed that LhARA be developed in two stages. In the first stage, a programme of *in vitro*
17 radiobiology will be served with proton beams with energies between 10 MeV and 15 MeV. In
18 stage two, the beam will be accelerated using a fixed-field alternating-gradient accelerator (FFA).
19 This will allow experiments to be carried out *in vitro* and *in vivo* with proton beam energies of up
20 to 127 MeV. In addition, ion beams with energies up to 33.4 MeV per nucleon will be available for
21 *in vitro* and *in vivo* experiments. This paper presents the conceptual design for LhARA and the
22 R&D programme by which the LhARA consortium seeks to establish the facility.

23 LAY SUMMARY

24 It is well established that radiation therapy (RT) is an effective treatment for many types of cancer.
25 Most treatments are delivered by machines that accelerate electrons which are then used to
26 produce a beam of high-energy photons (X-rays) which are directed at a tumour to kill cancer
27 cells. However, healthy tissue anywhere in the path of the photon beam is also irradiated and so
28 can be damaged. Modern X-ray therapy is able to reduce this damage by using several beams at
29 different angles.

30 Recent years have seen the use of a new type of machine in which protons are accelerated to
31 produce proton beams (rather than photon beams) which are directed at a tumour. These proton
32 beams can be arranged to deposit almost all of their energy in a small volume within a tumour so
33 they cause little damage to healthy tissue; a major advantage over photon beams. But proton
34 machines are large and expensive, so there is a need for the development of proton machines
35 that are smaller, cheaper and more flexible in how they can be used.

36 The LhARA project is aimed at the development of such proton machines using a new approach
37 based on high power lasers. Such new machines could also make it easier to deliver the dose in
38 very short high-intensity pulses and as a group of micro-beams—exciting recent research has
39 shown that this brings improved effectiveness in killing cancer cells while sparing healthy tissue.
40 The technology to be proved in LhARA should enable a course of RT to be delivered in days
41 rather than weeks.

42 Scientifically, there is a need to understand better the basic processes by which radiation
43 interacts with biological matter to kill cancer cells—the investigation of these processes involves
44 physics as well as biology. Thus the most important aim of LhARA is to pursue this radiobiological

45 research in new regimens and from this to develop better treatments. LhARA will also pursue
46 technological research into laser-hybrid accelerators.

47 **Keywords:** Radiobiology, Novel acceleration, Proton beam therapy, Ion beam therapy, Laser-driven acceleration, Plasma lens, Fixed
48 field alternating gradient acceleration

1 INTRODUCTION

49 Cancer is the second most common cause of death globally [The World Health Organisation (2020)]. In
50 2018, 18.1 million new cancer cases were diagnosed, 9.6 million people died of cancer-related disease, and
51 43.8 million people were living with cancer [Bray et al. (2018); Fitzmaurice et al. (2018)]. It is estimated
52 that 26.9 million life-years could be saved in low- and middle-income countries if radiotherapy capacity
53 could be scaled up [Atun et al. (2015)]. Novel techniques incorporated in facilities that are at once robust,
54 automated, efficient, and cost-effective are required to deliver the required scale-up in provision.

55 Radiation therapy (RT), a cornerstone of cancer treatment, is used in over 50 % of cancer patients [Datta
56 et al. (2019)]. The most frequently used types of radiotherapy employ photon or electron beams with
57 MeV-scale energies. Proton and ion beams offer substantial advantages over X-rays because the bulk
58 of the beam energy is deposited in the Bragg peak. This allows dose to be conformed to the tumour
59 while sparing healthy tissue and organs at risk. The benefits of proton and ion-beam therapy (PBT) are
60 widely recognised. PBT today is routinely delivered in fractions of ~ 2 Gy per day over several weeks;
61 each fraction being delivered at a rate of $\lesssim 5$ Gy/minute deposited uniformly over the target treatment
62 volume. There is evidence of therapeutic benefit when dose is delivered at ultra-high rate, $\gtrsim 40$ Gy/s, in
63 “FLASH” RT [Berry (1973); Favaudon et al. (2014); Durante et al. (2018); Vozenin et al. (2019); Wilson
64 et al. (2020b)] or when multiple micro-beams with diameter less than 1 mm distributed over a grid with
65 inter-beam spacing ~ 3 mm are used [Prezado and Fois (2013); Prezado et al. (2017b,a, 2018); González
66 and Prezado (2018); Martínez-Rovira et al. (2017)]. However, the radiobiological mechanisms by which
67 the therapeutic benefit is generated using these approaches are not entirely understood.

68 LhARA, the Laser-hybrid Accelerator for Radiobiological Applications, is conceived as the new, highly
69 flexible, source of radiation that is required to explore the mechanisms by which the biological response to
70 ionising radiation is determined by the physical characteristics of the beam. A high-power pulsed laser
71 will be used to drive the creation of a large flux of protons or ions which are captured and formed into a
72 beam by strong-focusing plasma lenses. The plasma (Gabor) lenses provide the same focusing strength
73 as high-field solenoids at a fraction of the cost. Rapid acceleration will be performed using a fixed-field
74 alternating-gradient accelerator (FFA), thereby preserving the unique flexibility in the time, energy, and
75 spatial structure of the beam afforded by the laser-driven source.

76 The LhARA facility may be developed in two stages. In the first stage, the laser-driven beam, captured
77 and transported using plasma lenses and bending magnets, will serve a programme of *in vitro* radiobiology
78 with proton beams of energy of up to 15 MeV. In stage two, the beam will be accelerated using an FFA. This
79 will allow experiments to be carried out *in vitro* and *in vivo* with proton-beam energies of up to 127 MeV.
80 Ion beams (including C^{6+}) with energies up to 33.4 MeV per nucleon will also be available.

81 The laser pulse that initiates the production of protons or ions at LhARA may be triggered at a repetition
82 rate of up to 10 Hz. The time structure of the beam may therefore be varied to interrupt the chemical
83 and biological pathways that determine the biological response to ionising radiation using 10 ns to 40 ns
84 long proton or ion bunches repeated at intervals as small as 100 ms. The technologies chosen to capture,
85 transport, and accelerate the beam in LhARA ensure that this unique capability is preserved. The LhARA
86 beam may be used to deliver an almost uniform dose distribution over a circular area with a maximum
87 diameter of between 1 cm and 3 cm. Alternatively, the beam can be focused to a spot with diameter of
88 ~ 1 mm.

89 The technologies that will be developed in LhARA have the potential to make particle-beam therapy
90 (PBT) available to the many. The laser-hybrid approach will allow radiobiological studies and eventually

91 radiotherapy to be carried out in completely new regimens, delivering a variety of ion species in a broad
92 range of time structures, spectral distributions, and spatial configurations at instantaneous dose rates up to
93 and potentially significantly beyond the current ultra-high dose-rate “FLASH” regime.

94 The “pre Conceptual Design Report” (pre-CDR) for LhARA [The LhARA consortium (2020)] lays the
95 foundations for the development of full conceptual and technical designs for the facility. The pre-CDR
96 also contains a description of the R&D that is required to demonstrate the feasibility of critical LhARA
97 components and systems. This paper presents a summary of the contents of the pre-CDR and lays out the
98 vision of the LhARA consortium.

99

2 MOTIVATION

100 RT delivered using protons and ions, particle-beam therapy (PBT), has the potential to overcome some of
101 the fundamental limitations of X-rays in cancer treatment through the targeted delivery of the radiation
102 dose [Loeffler and Durante (2013)]. The Particle Therapy Co-Operative Group (PTCOG) currently lists
103 90 proton therapy facilities and 12 carbon ion therapy facilities worldwide, located predominantly in
104 high-income countries [PTCOG (2020)]. Low- and middle-income countries (LMIC) are relatively poorly
105 served, indeed nearly 70% of cancer patients globally do not have access to RT [Datta et al. (2019)].

106 **The case for a systematic study of the radiobiology of proton and ion beams**

107 The efficacy of proton and ion beams is characterised by their relative biological effectiveness (RBE) in
108 comparison to a reference photon beam. The treatment-planning software that is in use in the clinic today
109 assumes an RBE value for protons of 1.1 [Paganetti and van Luijk (2013)], meaning that, compared to
110 X-rays, a lower dose of protons is needed to produce the same therapeutic effect. However, the rapid
111 rise in the linear energy transfer (LET) at the Bragg peak leads to significant uncertainties in the RBE.
112 Furthermore, it is known that RBE depends strongly on many factors, including particle energy, dose, dose
113 rate, the degree of hypoxia, and tissue type [Paganetti (2014)]. Indeed, RBE values from 1.1 to over 3 have
114 been derived from *in vitro* clonogenic-survival assay data following proton irradiation of cultured cell lines
115 derived from different tumours [Paganetti (2014); Chaudhary et al. (2014); Wilkens and Oelfke (2004)].
116 RBE values of ~ 3 are accepted for high-LET carbon-ion irradiation, although higher values have been
117 reported [Karger and Peschke (2017)]. RBE uncertainties for carbon and other ion species are at least as
118 large as they are for protons. These uncertainties can lead to an incorrect estimation of the dose required to
119 treat a particular tumour. Overestimation can lead to the damage of healthy tissue, while an underestimate
120 can lead to the tumour not being treated sufficiently for it to be eradicated.

121 The radio-therapeutic effect is caused largely by irreparable damage to the cell’s DNA. The spectrum
122 of DNA damage induced within tumour cells changes in response to differences in RBE. Larger RBE
123 values, corresponding to higher LET, can increase the frequency and complexity of DNA damage, in
124 particular causing DNA double-strand breaks (DSB) and complex DNA damage (CDD), where multiple
125 DNA lesions are induced in close proximity [Vitti and Parsons (2019); Carter et al. (2018)]. These DNA
126 lesions are a major contributor to radiation-induced cell death as they represent a significant barrier to
127 the cellular DNA-repair machinery [Vitti and Parsons (2019)]. However, a number of other biological
128 factors contribute to varying RBE in specific tumours, including the intrinsic radio-sensitivity of the
129 tissue, the level of oxygenation (hypoxia), the growth and re-population characteristics, and the associated
130 tumour micro-environment. Consequently, there is still significant uncertainty in the precise radiobiological
131 mechanisms that arise and how these mechanisms are affected by PBT. Detailed systematic studies of the
132 biophysical effects of the interaction of protons and ions, under different physical conditions, with different

133 tissue types will provide important information on RBE variation and could enable enhanced patient
134 treatment-planning algorithms to be devised. In addition, studies examining the impact of combination
135 therapies with PBT (e.g. targeting the DNA damage response, hypoxia signalling mechanisms and also the
136 tumour micro-environment) are currently sparse; performing these studies will therefore provide input vital
137 to the development of future personalised patient-therapy strategies using PBT.

138 **The case for novel beams for radiobiology**

139 Extending the range of beam characteristics used in PBT delivery may have significant therapeutic benefits.
140 Delivery of RT at high dose rates has led to noticeably reduced lung fibrosis in mice, skin toxicity in
141 mini-pigs, and reduced side-effects in cats with nasal squamous-cell carcinoma, effects currently thought
142 to be mediated via local oxygen depletion [Wilson et al. (2020b,a)]. In fact, the first patient with CD30+
143 T-cell cutaneous lymphoma has been safely treated with electrons delivered at FLASH dose rates [Bourhis
144 et al. (2019)]. In addition, therapeutic benefit has been demonstrated with the use of multiple micro-
145 beams [Prezado et al. (2017b)]. However, there is still significant uncertainty regarding the thresholds
146 and the radiobiological mechanisms underlying these effects. Extensive further study both *in vitro* and in
147 appropriate *in vivo* models is required.

148 The LhARA facility will provide access to proton and stable ion beams, provide a wide variety of
149 temporal, spatial, and spectral fractionation schemes, and deliver reliable and reproducible biological
150 data with fewer constraints than at current clinical centres. LhARA will allow direct radiobiological
151 comparisons of the effects of different charged particles at different energies and dose rates and enable
152 unique mechanistic studies (e.g. examination of the oxygen depletion hypothesis for FLASH). In addition,
153 LhARA will enable exhaustive evaluations of RBE using more complex end-points (e.g. angiogenesis and
154 inflammation) in addition to routine survival measurements. The ability to evaluate charged particles in
155 conjunction with other therapies (immunotherapy and chemotherapy) and to perform *in vivo* experiments
156 with the appropriate animal models is of great importance given the current lack of evidence in these areas.
157 LhARA therefore has the potential to provide the radiobiological data required to improve clinical practice.

158 The simulations of LhARA presented in this document have been used to estimate the dose delivered as a
159 function of energy for protons and carbon ions. These simulations, described in sections 3.3 and 3.4, show
160 instantaneous particle rates of the order of 10^9 particles per shot can be achieved, corresponding to average
161 dose rates of up to $\gtrsim 120$ Gy/s for protons and $\gtrsim 700$ Gy/s for carbon ions. These estimates are based on
162 the baseline specifications for LhARA.

163 **Laser-hybrid beams for radiobiology and clinical application**

164 High-power lasers have previously been proposed as an alternative to conventional proton and carbon-ion
165 facilities for radiotherapy [Bulanov et al. (2002); Fourkal et al. (2003); Malka et al. (2004)]. Laser-driven
166 sources have also been proposed as the basis for electron, proton and ion-beams for radiobiology [Kraft
167 et al. (2010); Fiorini et al. (2011); Yogo et al. (2011); Bin et al. (2012); Doria et al. (2012); Zeil et al.
168 (2013); Masood et al. (2014); Zlobinskaya et al. (2014)]. While a number of cell irradiation experiments
169 have been conducted with laser-accelerated ions [Doria et al. (2012); Zeil et al. (2013); Pommarel et al.
170 (2017); Manti et al. (2017)], these have been limited in scope to a single-shot configuration. More recent
171 projects (e.g. A-SAIL [A-SAIL Project (2020)], ELI [Cirrone et al. (2013)] and SCAPA [Wiggins et al.
172 (2019)]) will also investigate radiobiological effects using laser-driven ion beams. These studies will also
173 address various technological issues [Manti et al. (2017); Romano et al. (2016a); Masood et al. (2017);
174 Chaudhary et al. (2017); Margarone et al. (2018)].

175 A beam line to provide ion-driven beams for multi-disciplinary applications, ELIMAIA (ELI
176 Multidisciplinary Applications of laser-Ion Acceleration) is being brought into operation at the Extreme
177 Light Infrastructure (ELI) [Cirrone et al. (2020); Schillaci et al. (2019)]. This beam line will include the
178 “ELI MEDical and multidisciplinary applications” (ELIMED) beam line which will allow radiobiological
179 investigations to be carried out [Cirrone et al. (2016); Romano et al. (2016b); Milluzzo et al. (2017); Pipek
180 et al. (2017); Milluzzo et al. (2018); Cirrone et al. (2020)]. LhARA is distinguished from this facility in
181 that the energy at which the beam will be captured has been chosen to maximise the shot-to-shot stability
182 of the particle flux.

183 Protons and ions at conventional facilities are captured at energies of several tens of keV. At such low
184 energies, the mutual repulsion of the particles, the “space-charge effect”, limits the maximum instantaneous
185 dose rate. The laser-driven source allows protons and ions to be captured at significantly higher energies,
186 thus evading the current space-charge limit. Rapid acceleration will be performed using a fixed-field
187 alternating-gradient accelerator (FFA), thereby preserving the unique flexibility in the time, energy, and
188 spatial structure of the beam afforded by the laser-driven source. Modern lasers are capable of delivering a
189 Joule of energy in pulses that are tens of femtoseconds in length at repetition rates of $\gtrsim 10$ Hz. Laser-driven
190 ion sources create beams that are highly divergent, have a large energy spread, and an intensity that can vary
191 by up to 25% pulse-to-pulse [Dover et al. (2020)]. These issues are addressed in the LhARA conceptual
192 design through the use of Gabor lenses to provide strong focusing and to allow energy selection. In addition,
193 sophisticated instrumentation will be used in a fast feedback-and-control system to ensure that the dose
194 delivered is both accurate and reproducible. This approach will allow multiple ion species, from proton to
195 carbon, to be produced from a single laser by varying the target foil and particle-capture optics.

196 LhARA will prove the principle of the novel technologies required for the development of future therapy
197 facilities. The legacy of the LhARA programme will therefore be: a unique facility dedicated to the
198 development of a deep understanding of the radiobiology of proton and ion beams; and the demonstration
199 in operation of technologies that will allow PBT to be delivered in completely new regimens.
200

3 THE LHARA FACILITY

201 The LhARA facility, shown schematically in figure 1, has been designed to serve two end stations for
202 *in vitro* radiobiology and one end station for *in vivo* studies. The principle components of Stage 1 of the
203 LhARA accelerator are: the laser-driven proton and ion source; the matching and energy selection section;
204 beam delivery to the low-energy *in vitro* end station; and the low-energy abort line. Stage 2 is formed by
205 the injection line for the fixed-field alternating-gradient accelerator (FFA); the FFA; the extraction line; the
206 high-energy abort line; beam delivery to the high-energy *in vitro* end station; and the transfer line to the *in*
207 *vivo* end station. Proton beams with energies of between 12 MeV and 15 MeV will be delivered directly
208 from the laser-driven source to the low-energy *in vitro* end station via a transfer line. The high-energy *in*
209 *vitro* end station and the *in vivo* end station will be served by proton beams with energy between 15 MeV
210 and 127 MeV and by ion beams, including C^{6+} with energies up to 33.4 MeV/u. The design parameters
211 for the various components of LhARA are given in tables 1 and 2. The design of the LhARA facility is
212 described in the sections that follow.

213

3.1 Laser-driven proton and ion source

214 A novel solution for proton and ion acceleration is to use a compact, flexible laser-driven source coupled to
215 a state-of-the-art beam-transport line. This allows an accelerating gradient of $\gtrsim 10$ GV/m to be exploited
216

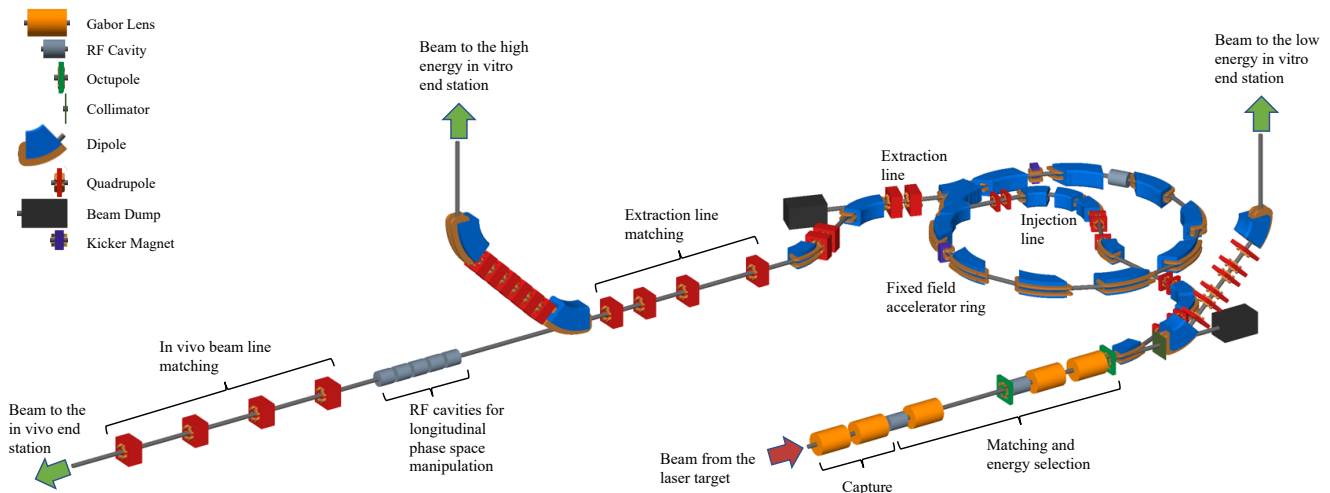


Figure 1. Schematic diagram of the LhARA beam lines. The particle flux from the laser-driven source is shown by the red arrow. The ‘Capture’ section is followed by the ‘Matching and energy selection’ sections, the beam is directed either into the 90° bend that takes it to the low-energy *in vitro* end station, towards the FFA injection line, or to the low-energy beam dump. Post acceleration is performed using the FFA, on extraction from which the beam is directed either to the high-energy *in vitro* end station, the *in vivo* end station, or the high-energy beam dump. Gabor lenses are shown as orange cylinders, RF cavities as grey cylinders, octupole magnets as green discs, collimators as dark-green bars, dipole magnets are shown in blue, quadrupole magnets are shown in red, beam dumps (black rectangles) and kicker magnets are also shown.

217 at the laser-driven source. We propose to operate in the laser-driven sheath-acceleration regime [Clark et al.
 218 (2000a); Snively et al. (2000); Daido et al. (2012)] for ion generation. An intense, short laser pulse will
 219 be focused onto a target. The intense electric field generated on the front surface of the target accelerates
 220 the surface electrons, driving them into the material. Electrons which gain sufficient energy traverse the
 221 target, ionising the material as they go. A strong space-charge electric field, the ‘sheath’, is created as
 222 the accelerated electrons exit the rear surface of the target. This field in turn accelerates protons and ions
 223 present as contaminants on the surface. The sheath-acceleration scheme has been shown to produce ion
 224 energies greater than 40 MeV/u at the highest laser intensities [Dover et al. (2020)]. The maximum proton
 225 energy (E_p) scales with laser intensity (I) as, $E_p \propto I^{\frac{1}{2}}$. The laser required to deliver a significant proton
 226 flux at 15 MeV is commercially available.

227 The distribution of proton and ion energies observed in laser-driven beams exhibits a sharp cut-off at
 228 the maximum energy and, historically, the flux of laser-accelerated ion beams has varied significantly
 229 shot-to-shot. To reduce these variations, the choice has been made to select particles from the plateau of
 230 the two-temperature energy spectrum of the laser-accelerated ion beam [Clark et al. (2000b); Passoni et al.
 231 (2010)]. This should enhance ion-beam stability and allow reproducible measurements to be carried out at
 232 ultra-high dose rates using a small number of fractions. To create the flux required in the plateau region,
 233 it is proposed that a 100 TW laser system is used. A number of commercial lasers are available that are
 234 capable of delivering > 2.5 J in pulses of duration < 25 fs, at 10 Hz with contrast better than $10^{10} : 1$.
 235 Shot-to-shot stability of $< 1\%$ is promised, an important feature for stable ion-beam production.

236 Target

237 Key to the operation of this configuration is a system that refreshes the target material at high repetition-rate

Table 1. Design parameters of the components of the LhARA facility. The parameter table is provided in a number of sections. This section contains parameters for the Laser-driven proton and ion source, the Proton and ion capture section, and the Stage 1 beam transport section.

Parameter	Value or range	Unit
Laser driven proton and ion source		
Laser power	100	TW
Laser Energy	2.5	J
Laser pulse length	25	fs
Laser rep. rate	10	Hz
Required maximum proton energy	15	MeV
Proton and ion capture		
Beam divergence to be captured	50	mrad
Gabor lens effective length	0.857	m
Gabor lens length (end-flange to end-flange)	1.157	m
Gabor lens cathode radius	0.0365	m
Gabor lens maximum voltage	65	kV
Number of Gabor lenses	2	
Alternative technology: solenoid length	1.157	m
Alternative technology: solenoid max field strength	1.3	T
Stage 1 beam transport: matching & energy selection, beam delivery to low-energy end station		
Number of Gabor lenses	3	
Number of re-bunching cavities	2	
Number of collimators for energy selection	1	
Arc bending angle	90	Degrees
Number of bending magnets	2	
Number of quadrupoles in the arc	6	
Alternative technology: solenoid length	1.157	m
Alternative technology: solenoid max field strength (to serve the injection line to the Stage 2)	0.8 (1.4)	T

238 in a reproducible manner. A number of schemes have been proposed for such studies, including high-
 239 pressure gases [Willingale et al. (2009); Bin et al. (2015); Chen et al. (2017)], cryogenic hydrogen ribbons
 240 [Margarone et al. (2016); Gauthier et al. (2017); Obst et al. (2017)], liquid sheets [Morrison et al. (2018)]
 241 and tape drives [Noaman-ul Haq et al. (2017)]. For LhARA, a tape drive based on the system developed at
 242 Imperial College London is proposed [Dover et al. (2020)]. This system is capable of reliable operation at
 243 target thicknesses down to $5\ \mu\text{m}$, using aluminium or steel foils, and down to $18\ \mu\text{m}$ using plastic tapes.
 244 Such tape-drive targets can be operated at high charge (up to 100 pC at $15 \pm 1\ \text{MeV}$, i.e. $> 10^9$ protons per
 245 shot) and can deliver high-quality proton and ion fluxes at repetition rates of up to 10 Hz or greater.

246 The careful control of the tension of the tape in a tape-drive target is critical for reproducible operation. The
 247 tape must be stretched enough to flatten the surface, but not enough to cause plastic deformations. Surface
 248 flatness is important for a number of reasons. Rippling of the front surface modifies the laser absorption
 249 dramatically; uncharacterised rippling can make shot-to-shot variations significant and unpredictable
 250 [Noaman-ul Haq et al. (2017)]. Similarly, rear surface perturbations can modify the sheath field, resulting
 251 in spatial non-uniformities of the proton beam or suppression of the achievable peak energies. Tape drives
 252 with torsion control and monitoring to maintain a high-quality tape surface have been designed and operated
 253 in experiments at Imperial College London. The development of these targets continues with a view to the
 254 production of new, thinner tapes for improved ion generation and the creation of ion species other than

Table 2. Design parameters of the components of the LhARA facility. The parameter table is provided in a number of sections. This section contains parameters for the Stage 2 beam transport and the *in vitro* and *in vivo* end stations.

Parameter	Value or range	Unit
Stage 2 beam transport: FFA, transfer line, beam delivery to high-energy end stations		
Number of bending magnets in the injection line	7	
Number of quadrupoles in the injection line	10	
FFA: Machine type	single spiral scaling FFA	
FFA: Extraction energy	15–127	MeV
FFA: Number of cells	10	
FFA: Orbit R_{\min}	2.92	m
FFA: Orbit R_{\max}	3.48	m
FFA: Orbit excursion	0.56	m
FFA: External R	4	m
FFA: Number of RF cavities	2	
FFA: RF frequency	1.46–6.48	MHz
FFA: harmonic number	1, 2 or 4	
FFA: RF voltage (for 2 cavities)	4	kV
FFA: spiral angle	48.7	Degrees
FFA: Max B field	1.4	T
FFA: k	5.33	
FFA: Magnet packing factor	0.34	
FFA: Magnet opening angle	12.24	degrees
FFA: Magnet gap	0.047	m
FFA: Ring tune (x,y)	(2.83,1.22)	
FFA: γ_T	2.516	
FFA: Number of kickers	2	
FFA: Number of septa	2	
Number of bending magnets in the extraction line	2	
Number of quadrupoles in the extraction line	8	
Vertical arc bending angle	90	Degrees
Number of bending magnets in the vertical arc	2	
Number of quadrupoles in the vertical arc	6	
Number of cavities for longitudinal phase space manipulation	5	
Number of quadrupoles in the <i>in vivo</i> beam line	4	
<i>In vitro</i> biological end stations		
Maximum input beam diameter	1-3	cm
Beam energy spread (full width)	Low-energy end station: ≤ 4 High-energy end station: ≤ 1	% %
Input beam uniformity	< 5	%
Scintillating fibre layer thickness	0.25	mm
Air gap length	5	mm
Cell culture plate thickness	1.3	mm
Cell layer thickness	0.03	mm
Number of end stations	2	
<i>In vivo</i> biological end station		
Maximum input beam diameter	1-3	cm
Beam energy spread (full width)	≤ 1	%
Input beam uniformity	< 5	%
Beam options	Spot-scanning, passive scattering, micro-beam	

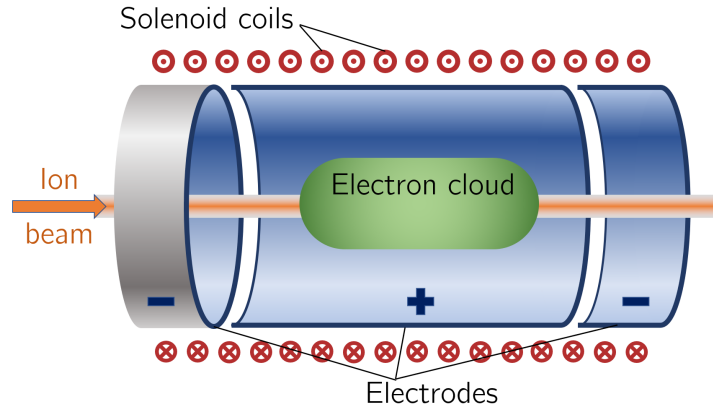


Figure 2. Schematic diagram of a Penning-Malmberg trap of the type proposed for use in the Gabor lenses to be used in LhARA. The solenoid coils, and the direction of current flow, are indicated by the red circles (the central dots indicate current emerging from the picture, crosses current entering it). The confining electrostatic potential is provided using a central cylindrical anode and two cylindrical negative end electrodes. The ion beam enters on-axis from the left and the electron cloud is indicated by the green shaded area.

255 protons and carbon. This is an active area of R&D that will continue with the development of LhARA.

256
257

3.2 Proton and ion capture

258 The use of an electron cloud as a focusing element for charged-particle beams was first proposed by
259 Gabor [Gabor (1947)]. The electron cloud is confined within the lens using a long cylindrical anode placed
260 within a uniform solenoid field, see figure 2. Such a configuration is commonly known as a ‘Penning
261 trap’ and has found wide application in many fields [Thompson (2015)]. Variations on the Penning trap
262 where axial apertures in the cathodes are introduced, such as the Penning-Malmberg trap [deGrassie and
263 Malmberg (1980); Malmberg et al. (1988)] are attractive for beam-based applications due to the excellent
264 access provided to the plasma column.

265 The focal length of a Gabor lens of length l is given in terms of the electron number density by:

$$\frac{1}{f} = \frac{e^2 n_e}{4\epsilon_0 U} l; \quad (1)$$

266 where e is the magnitude of the electric charge of the electron, n_e is the number density of the electrons
267 confined within the lens, ϵ_0 the permittivity of free space, and U the kinetic energy of the particle beam.
268 The desired focusing strength determines n_e which in turn allows the anode voltage and magnetic-field
269 strength to be calculated [Reiser (1989); Pozimski and Aslaninejad (2013)]. The focal lengths required to
270 capture the proton and ion beams at LhARA have been chosen such that the necessary electron number
271 densities lie well within the range achieved in published experiments.

272 For a given focal length, the magnetic field strength required in the Gabor lens is smaller than that of
273 a solenoid that would give equivalent focusing. In the non-relativistic approximation, the relationship
274 between the magnetic field strength in the Gabor lens, B_{GBL} , and the equivalent solenoid, B_{sol} , is given

275 by [Pozimski and Aslaninejad (2013)]:

$$B_{\text{GPL}} = B_{\text{sol}} \sqrt{Z \frac{m_e}{m_p}}; \quad (2)$$

276 where Z is the charge state of the ions. In the case of a proton beam, the reduction factor is 43. This means
277 the cost of the solenoid for a Gabor lens can be significantly lower than the cost of a solenoid of equivalent
278 focusing strength.

279 Instability of the electron cloud is a concern in the experimental operation of a Gabor lens; azimuthal
280 beam disruption due to the diocotron instability has been observed and described theoretically [Meusel et al.
281 (2013)]. Theory indicates that the diocotron instability is most problematic under well-defined geometric
282 conditions. The reliable operation of a Gabor lens in a regime free from this instability has yet to be
283 demonstrated. Gabor lenses promise very strong focusing, simple construction, and low magnetic field,
284 all attractive features for LhARA. However, these attractive features come at the cost of relatively high
285 voltage operation ($\gtrsim 50$ kV) and possible vulnerability to instability.

286 With reliable operation of Gabor lenses as yet unproven, we plan a two-part experimental and theoretical
287 programme of research to investigate their Gabor suitability. Initial work will include: the theoretical study
288 of lens stability using a full 3D particle-in-cell code such as VSIM [VSI (2020)]; and the development of
289 electron-density diagnostics based on interferometric measurement of the resulting refractive-index change.
290 A test Gabor lens will be constructed to allow validation of both the simulation results and a new diagnostic
291 tool using an alpha emitter as a proxy for the LhARA beam. In addition, the initial investigation will
292 include the design of an injection system to fill the lens with the required electron cloud. Should it prove
293 impossible to produce a suitable Gabor lens, it will be necessary to use high-field solenoids to produce the
294 equivalent focusing effect.

295

296 **3.3 Beam transport and delivery to the low-energy *in vitro* end station**

297 The beam transport line to the low-energy *in vitro* end station must produce a uniform dose distribution at
298 the cell layer. Beam losses must be minimised for radiation safety and to maximise the dose that can be
299 delivered in a single shot. The transport line has been designed to minimise regions in which the beam
300 is brought to a focus to reduce the impact of space-charge forces on the beam phase-space. An optical
301 solution was initially developed using Beamoptics [Autin et al. (1998)] and MADX [Grote and Schmidt
302 (2003)]. Accurate estimation of the performance of the beam line requires the inclusion of space-charge
303 forces and particle-matter interactions. Performance estimation was therefore performed using Monte Carlo
304 particle-tracking from the ion source to the end station. BDSIM [Nevay et al. (2020)], which is based on
305 the GEANT4 toolkit, was used for the simulation of energy deposition arising from beam interactions with
306 the material in the accelerator and the end station. GPT [De Loos and Van der Geer (1996)] was used for
307 evaluating the full 3D impact of space-charge effects.

308 An idealised Gaussian beam was generated with a spot size of $4 \mu\text{m}$ FWHM, an angular divergence of
309 50 mrad, 35 fs FWHM bunch length, and an energy spread of 1×10^{-6} MeV. The maximum estimated
310 bunch charge is 1×10^9 protons. The presence of a substantial electron flux produced from the laser target
311 compensates the high proton charge density in the vicinity of the ion-production point. To approximate the
312 partial space-charge compensation in this region, it was assumed that co-propagating electrons would fully
313 compensate the space-charge forces over the first 5 cm of beam propagation. Beyond this, the proton beam
314 was assumed to have separated from the co-propagating electrons sufficiently for space-charge to become

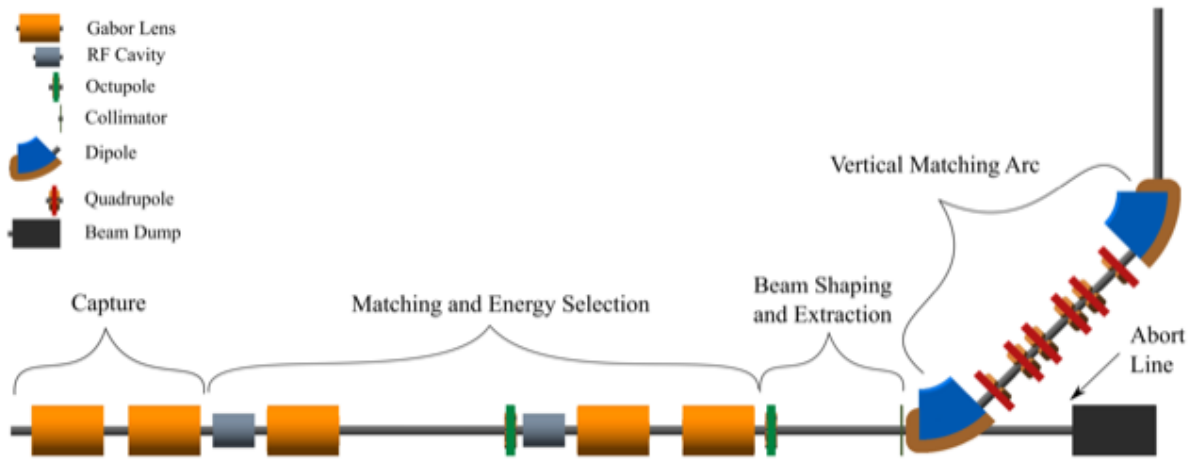


Figure 3. Beam transport for Stage 1 of LhARA visualised in BDSIM, showing five machine sections. The capture section is composed of two Gabor lenses (orange cylinders). The matching and energy selection section includes three Gabor lenses, two RF cavities (grey cylinders) and an octupole magnet (green disc). The beam shaping and extraction section includes a second octupole and a collimator (vertical dark-green bar). The vertical matching arc directs the beam into the low-energy *in vitro* end station and is composed of two 45° dipoles (blue and brown) and six quadrupoles (red). The total length of this beam line is 17.3 m.

315 a significant effect and cause emittance growth. Therefore, a further 5 cm drift was simulated including
 316 space-charge forces. At a distance of 10 cm from the ion source, the beam is at the exit of the laser-target
 317 vessel. The kinematic distributions of ions in the beam were stored at this point and passed to the relevant
 318 BDSIM and GPT simulations of the downstream beam line.

319 The Stage 1 beam line, shown schematically in figure 3, is composed of five sections: beam capture;
 320 matching and energy selection; beam shaping; vertical arc matching; and an abort line. The capture section
 321 uses two Gabor lenses to minimise the transverse momentum of particles in the beam. Beyond the capture
 322 section, an RF cavity permits control of the bunch length and manipulation of the longitudinal phase-space.
 323 A third Gabor lens then focuses the bunch to a small spot size after which a second RF cavity is located
 324 to provide further longitudinal phase-space manipulation. Two further Gabor lenses ensure the beam is
 325 again parallel before it enters the vertical 90° arc. All Gabor lenses have an inner radius of 3.65 cm and an
 326 effective length of 0.857 m. All lenses operate at a cathode voltage of less than 65 kV.

327 The parallel beam that emerges from the final Gabor lens, provides significant flexibility for the inclusion
 328 of beam shaping and extraction systems. Beam uniformity will be achieved using octupole magnets to
 329 provide third-order focusing to perturb the first-order focusing of the Gabor lenses. Such schemes have
 330 been demonstrated in magnetic lattices in a number of facilities [Tsoupas et al. (1991); Urakabe et al.
 331 (1999); Amin et al. (2018)]. A suitable position for the first octupole was identified to be after the final
 332 Gabor lens where the beam is large; its effect on the beam is expected to be significant. Octupoles were
 333 only modelled in BDSIM, as GPT does not have a standard component with an octupolar field. The typical
 334 rectangular transverse distribution resulting from octupolar focusing requires collimation to match the
 335 circular aperture through which the beam enters the end station. A collimator is therefore positioned at the
 336 start of the vertical arc. Further simulations are required to determine the optimum position of the second
 337 octupole and to evaluate the performance of the octupoles. The switching dipole which directs the beam to
 338 the injection line of the FFA in Stage 2 will be located between the second octupole and the collimator,
 339 requiring the octupole to be ramped down for Stage 2 operation.

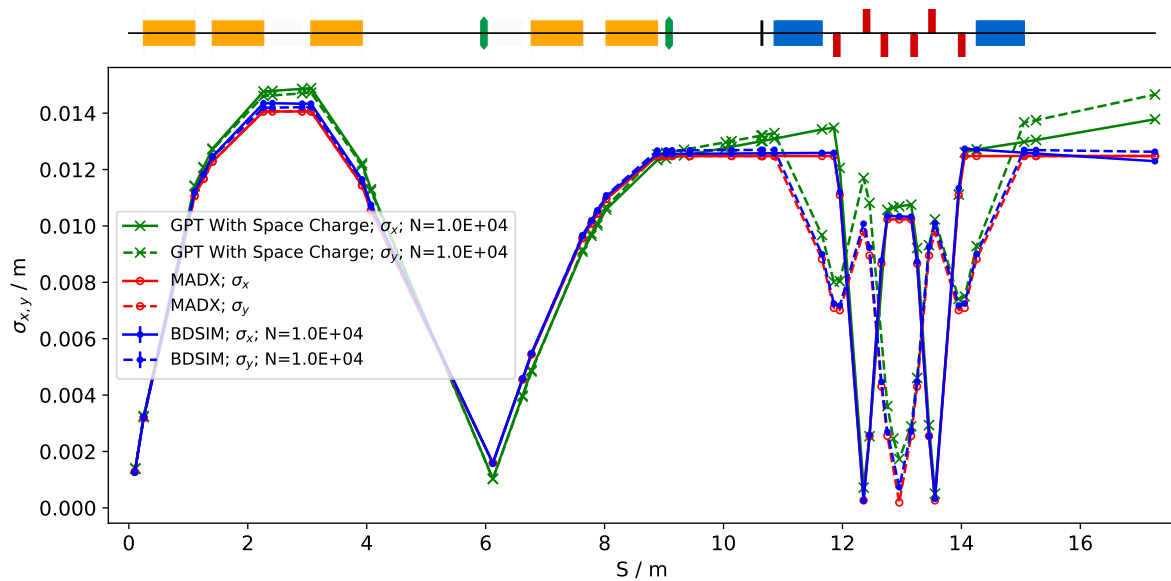


Figure 4. Horizontal (solid lines) and vertical (dashed lines) beam sizes through the *in vitro* beam transport, simulated including space-charge effects in GPT (green), and without space-charge in MADX (red) and BDSIM (blue).

340 The vertical arc uses transparent optics in an achromat matching section to ensure that the first-order
 341 transfer map through the arc is equivalent to the identity transformation and that any dispersive effects
 342 are cancelled. A 2 m drift tube is added after the arc to penetrate the concrete shielding of the end station
 343 floor and to bring the beam to bench height. The abort line consists of a drift space followed by a beam
 344 dump. Ramping down the first vertical dipole causes the beam to enter the dump and prevents particle
 345 transportation to the end station.

346 The underlying physics of plasma-lens operation cannot be simulated in BDSIM or GPT. It can, however,
 347 be approximated using solenoid magnets of equivalent strength. RF cavity fields were not simulated.

348 To produce the results shown here, 10 000 particles were simulated, corresponding to the estimated
 349 maximum bunch charge of 1×10^9 protons. Figure 4 shows excellent agreement between horizontal and
 350 vertical transverse beam sizes in BDSIM and MADX, verifying the beam line's performance in the absence
 351 of space-charge effects. Reasonable agreement between BDSIM and GPT is also seen when space-charge
 352 forces are included in GPT. Emittance growth is observed prior to the first solenoid, affecting the optical
 353 parameters throughout the machine. However, the resulting beam dimensions at the cell layer of 1.38 cm
 354 horizontally and 1.47 cm vertically are not significantly different from those in BDSIM. If needed, further
 355 adjustments of the Gabor lens and arc-quadrupole strengths may compensate for any space-charge effects.
 356 The transmission efficiency of the beam line is approximately 100%.

357 The small bunch dimensions in both transverse planes at the focus after the third Gabor lens, where
 358 the energy selection collimator will be placed, could be of concern if the effect of space-charge has been
 359 underestimated. Similar bunch dimensions are achieved in the vertical arc. Here, however, quadrupolar
 360 focusing is confined to a single plane to mitigate possible further emittance growth.

361 To investigate beam uniformity, BDSIM simulations with and without octupoles and collimation for
 362 beam shaping were conducted. Each octupole was assumed to have a magnetic length of 0.1 m and pole-tip
 363 radius of 5 cm. The strength parameter, k_3 , of each octupole was arbitrarily set to 6000. A 2 cm thick iron

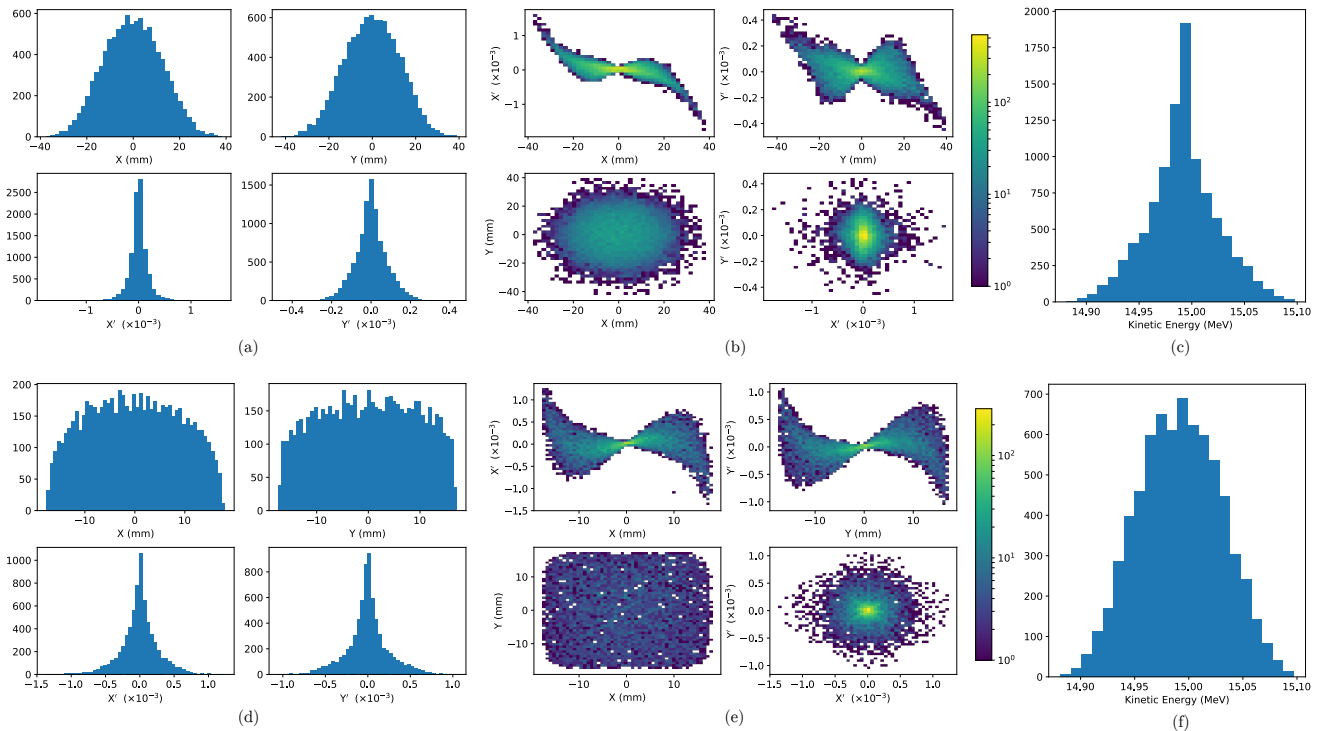


Figure 5. Beam phase space distributions at the end-station in the transverse plane, (X, Y) ; X' and Y' give the slope relative to the Z axis. The transverse phase space is shown in figures a and b for simulations without octupolar focusing and collimation, with the kinetic energy distribution shown in c. The same phase space distributions simulated with the effect of octupoles and collimation are in figures d, e, and f.

364 collimator with a 40 mm diameter aperture was positioned 1.5 m downstream of the octupole. Figure 5
 365 shows the beam phase-space and particle distributions at the Stage 1 end station for the transverse and
 366 longitudinal axes with and without beam shaping. Without octupoles, the spatial profile is Gaussian, as
 367 expected. Inclusion of the octupoles and collimation system improves beam uniformity. The total beam
 368 width is 3.58 cm horizontally and 3.46 cm vertically, which is sufficient to irradiate one well in a six-well
 369 cell-culture plate. Further optimisation is required to improve uniformity whilst optimising beam-line
 370 transmission, which is approximately 70% for the results presented in figure 5.

371 An aberration can be seen in both transverse planes with and without beam shaping. This effect originates
 372 upstream of the octupoles in the solenoids used to approximate the Gabor lenses, and persists to the
 373 end station. The aberration is a concern, but is likely to change when the solenoids are replaced by full
 374 electromagnetic simulation of the Gabor lenses, at which point it will be further investigated.

375 The non-Gaussian energy distribution without beam shaping is a result of space-charge forces at the
 376 ion source; the distribution persists to the end station as no components which affect the longitudinal
 377 phase space were simulated. The Gaussian distribution seen with beam shaping reflects the effects of the
 378 collimation.

379 The proposed design is capable of delivering beams of the desired size to the *in vitro* end station. Space-
 380 charge effects affect the beam-transport performance but it is believed that these can be mitigated with
 381 minor adjustments to the Gabor lenses in the capture section. Initial studies indicate that a uniform beam
 382 can be delivered with further optimisation of the octupoles and collimator.

383

384 3.3.1 Alternative Design

385 To mitigate potential emittance growth from space-charge forces, an alternative beam line design was
386 developed in which the final two Gabor lenses in the matching and energy selection section are replaced by
387 four quadrupoles, limiting any bunch focusing to one plane at a time. The resulting machine is reduced
388 in length to 15.4 m. Without space-charge effects, a beam width of 2.5 mm at the end station can be
389 achieved. With space-charge, emittance growth prior to the first solenoid is once again observed leading
390 to an increased beam size at the entrance of the first quadrupole, resulting in a spatially asymmetric and
391 divergent beam at the end station. It is believed that the space-charge effects can be compensated by
392 applying the same Gabor lens optimisation as in the baseline design and adjusting the quadrupole settings
393 to deliver beam parameters similar to those achieved in the absence of space charge. The alternative design
394 provides a solution that is more resilient to space-charge effects than the baseline, however, only the lower
395 bound on the desired beam size has been achieved so far. For this design, further optimisation is required
396 not only to improve optical performance but also to optimise octupole settings and to determine whether a
397 beam with the desired uniformity can be delivered to the end station.

398

399 3.4 Post-acceleration and beam delivery to the *in vitro* and *in vivo* end stations

400 A fixed-field alternating-gradient accelerator (FFA), based on the spiral scaling principle [Krest et al.
401 (1956); Symon et al. (1956); Fourier et al. (2008); Tanigaki et al. (2006)], will be used to accelerate the
402 beam in LhARA Stage 2 to obtain energies greater than the 15 MeV protons and 4 MeV/u carbon (C^{6+})
403 ions delivered by the laser-driven source. FFAs have many advantages for both medical and radiobiological
404 applications such as: the capability to deliver high and variable dose; rapid cycling with repetition rates
405 ranging from 10 Hz to 100 Hz or beyond; and the ability to deliver various beam energies without the use
406 of energy degraders. An FFA is relatively compact due to the use of combined function magnets, which
407 lowers the overall cost compared to conventional accelerators capable of delivering beams at a variety of
408 energies such as synchrotrons. Extraction can be both simple and efficient and it is possible for multiple
409 extraction ports to be provided. Furthermore, FFAs can accelerate multiple ion species, which is very
410 important for radiobiological experiments and typically very difficult to achieve with cyclotrons.

411 A typical FFA is able to increase the beam momentum by a factor of three, though a greater factor may
412 be achieved. For LhARA, this translates to a maximum proton-beam energy of 127 MeV from an injected
413 beam of 15 MeV. For carbon ions (C^{6+}) with the same rigidity, a maximum energy of approximately
414 33.4 MeV/u can be produced.

415 The energy at injection into the FFA determines the beam energy at extraction. The injection energy will
416 be changed by varying the focusing strengths in the Stage 1 beam line from the capture section through to
417 the extraction line and the FFA ring. Appropriate adjustments to the frequency and phase of the RF in the
418 FFA ring will also be made. This will allow the required energy slice from the broad spectrum produced at
419 the laser-driven source to be captured and transported to the FFA. The FFA will then accelerate the beam,
420 acting as a three-fold momentum multiplier. This scheme simplifies the injection and extraction systems
421 since their geometry and location can be kept constant.

422 A second, 'high-energy', *in vitro* end station will be served by proton beams with a kinetic energy in the
423 range 15–127 MeV and carbon-ion beams with energies up to 33.4 MeV/u. The extraction line from the
424 FFA leads to a 90° vertical arc to send the beam to the high-energy *in vitro* end station. If the first dipole of
425 the arc is not energised, the beam will be sent to the *in vivo* end station. The extraction line of the FFA
426 includes a switching dipole that will send the beam to the high-energy-beam dump if it is not energised.
427 The detailed design of the high-energy abort line, taking into account the requirement that stray radiation

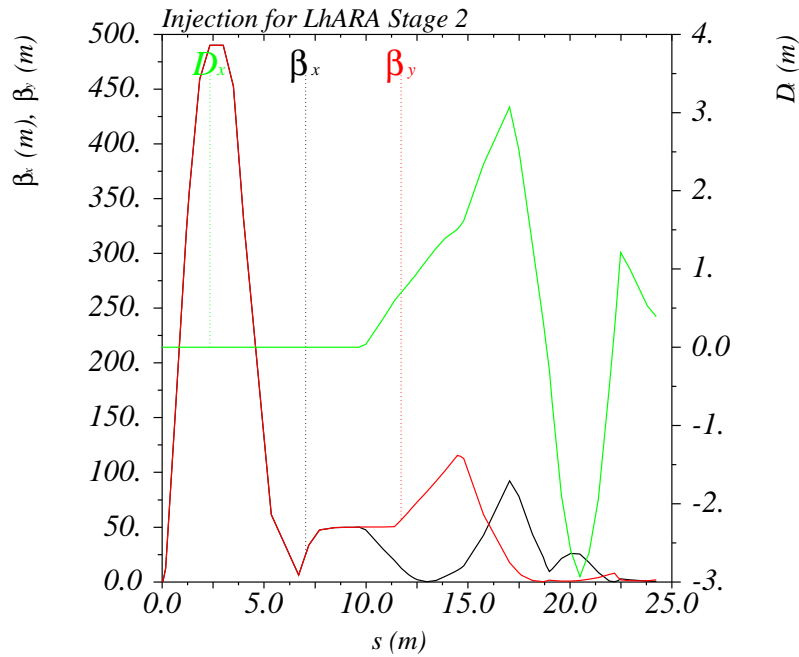


Figure 6. Twiss β_x and β_y functions and dispersion in the beam line consisting of the modified Stage 1 lattice and the transfer line allowing injection of the beam into the FFA ring. The distance s runs from the laser target to the exit of the injection septum.

428 does not enter the end stations, will be performed as part of the LhARA R&D programme.

429

430 3.4.1 Injection line

431 In order to inject the beam into the FFA, the settings of the Stage 1 beam line need to be adjusted to reduce
 432 the Twiss β function. The required Stage 1 optical parameters are shown in figure 6. The beam is diverted
 433 by a switching dipole into the injection line which transports the beam to the injection septum magnet.
 434 The injection line matches the Twiss β functions in both transverse planes and the dispersion of the beam
 435 to the values dictated by the periodic conditions in the FFA cell (figure 6). The presence of dispersion in
 436 the injection line allows a collimator to be installed for momentum selection before injection. The beam
 437 is injected from the inside of the ring, which requires that the injection line crosses one of the straight
 438 sections between the FFA magnets, see figure 7.

439

440 3.4.2 FFA ring

441 The magnetic field, B_y , in the median plane of a scaling spiral FFA is given by [Krest et al. (1956); Symon
 442 et al. (1956); Fourier et al. (2008)]:

$$B_y = B_0 \left[\frac{R}{R_0} \right]^k F \left(\theta - \ln \left[\frac{R}{R_0} \right] \tan \zeta \right); \quad (3)$$

443 where B_0 is the magnetic field at radius R_0 , k is the field index, ζ corresponds to the spiral angle and F is
 444 the ‘flutter function’. This field law defines a zero-chromaticity condition, which means the working point

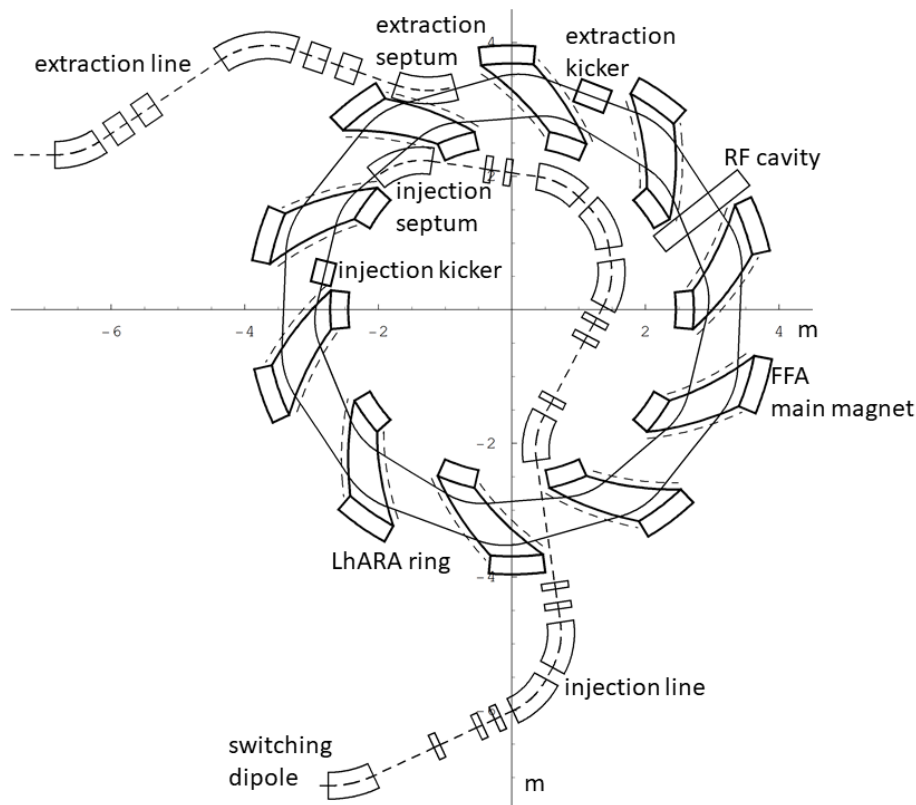


Figure 7. The layout of the injection line from the switching dipole to the injection septum together with the FFA ring, some of its subsystems and the first part of the extraction line.

445 of the machine is independent of energy (up to field errors and alignment imperfections). This avoids the
 446 need to cross any resonances, which would reduce the beam quality and could lead to beam loss.

447 Table 2 gives the main design parameters of the FFA ring. The ring consists of ten symmetric cells, each
 448 containing a single combined-function spiral magnet. The choice of the number of cells is a compromise
 449 between the size of the orbit excursion, which dictates the radial extent of the magnet, and the length of the
 450 straight sections required to accommodate the injection and extraction systems.

451 The betatron functions and dispersion in one lattice cell at injection are shown in figure 8(a). The tune
 452 diagram, showing the position of the working point of the machine in relation to the main resonance lines,
 453 is shown in figure 8(b). Tracking studies were performed using a step-wise tracking code in which the
 454 magnetic field is integrated using a Runge-Kutta algorithm [Lagrange et al. (2018)]. The magnetic field
 455 in the median plane was obtained using the ideal scaling law (equation 3). Enge functions were used to
 456 give the fringe fields. The field out of the median plane was obtained using Maxwell's equations and a
 457 6th-order Taylor expansion of the field. The dynamic acceptance for 100 turns, shown for the horizontal
 458 and vertical planes in figures 8(c) and 8(d), respectively, is significantly larger than the beam emittance.
 459 This statement holds even for the pessimistic scenario in which the emittance is assumed to be ten times
 460 larger than nominal. These results confirm that a good machine working point has been chosen.

461 A full aperture, fast injection of the beam will be performed using a magnetic septum, installed on the
 462 inside of the ring, followed by a kicker magnet situated in a consecutive lattice cell, as shown in figure 7.
 463 The specifications of the injection system are dictated by the parameters of the beam at injection, which are
 464 summarised for the nominal proton beam in table 3. The beam at injection has a relatively small emittance

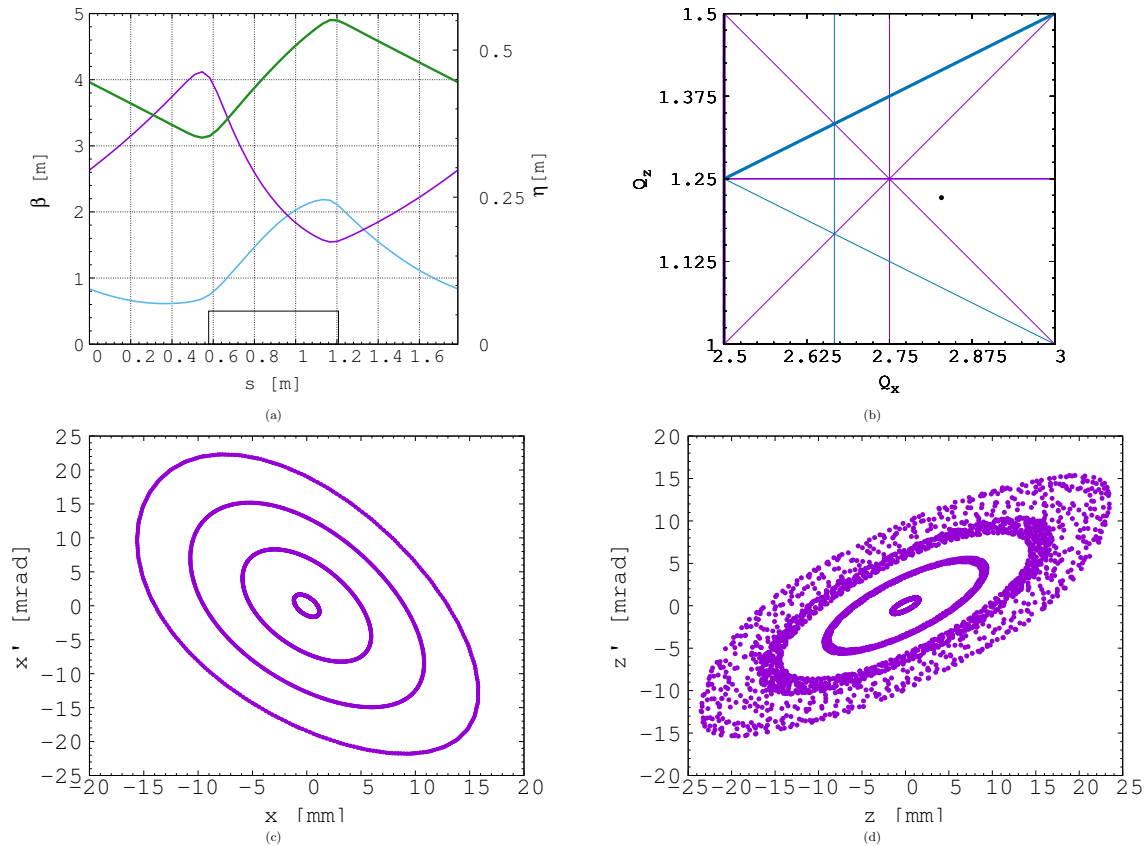


Figure 8. Beam optics and tracking in the FFA. Twiss β_h (blue), β_v (purple) functions and dispersion (green) in one lattice cell of the FFA ring (a). The working point of the FFA ring at (2.83, 1.22) on the tune diagram (b). The results of the horizontal (c) and vertical (d) dynamical acceptance study in the FFA ring, where a 1 mm offset is assumed in the vertical and horizontal planes respectively.

Table 3. Summary of the main parameters for the proton beam at the injection to the FFA ring. These parameters correspond to the nominal (maximum) acceleration mode of operation.

Parameter	Unit	Value
Beam energy	MeV	15
Total relative energy spread	%	± 2
Nominal physical RMS emittance (both planes)	π m rad	4.1×10^{-7}
Incoherent space charge tune shift		-0.8
Bunching factor		0.023
Total bunch length	ns	8.1
Bunch intensity		10^9

465 and short bunch length, which limits the intensity accepted by the ring due to the space-charge effect. An
 466 intensity of approximately 10^9 protons will be accepted by the ring assuming the nominal beam parameters.
 467 Space-charge effects will be severe immediately after injection, but will quickly be reduced due to the
 468 debunching of the beam. Fast extraction of the beam over the full aperture will be performed using a kicker
 469 magnet followed by a magnetic septum installed in a consecutive lattice cell close to the extraction orbit.

470 Acceleration of the beam to 127 MeV will be done using an RF system operating at harmonic number
 471 $h = 1$ with an RF frequency range from 2.89 MHz to 6.48 MHz. The RF voltage required for 10 Hz

Table 4. Beam emittance values and target β values for different beam sizes for 40 MeV and 127 MeV beams. The beam size is taken to be four times the sigma of the transverse beam distribution.

	40 MeV protons (Nominal)	127 MeV protons (Nominal)	127 MeV protons (Pessimistic)
RMS Emittance (ϵ_x, ϵ_y) [π mm mrad]	0.137	0.137	1.37
β [m] for a 1 mm spot size	0.46	0.46	0.039
β [m] for a 10 mm spot size	46	46	4.5
β [m] for a 30 mm spot size	410	410	40

472 operation is 0.5 kV. However, at this relatively low voltage the energy acceptance at injection is $\pm 0.7\%$.
 473 Operating with a voltage of 4 kV increases the energy acceptance to $\pm 2\%$. This voltage can be achieved
 474 with one cavity [Yonemura et al. (2008)]. Here, two cavities are proposed to provide greater operational
 475 stability. Normal conducting spiral-scaling FFA magnets, similar to the ones needed for LhARA, have been
 476 successfully constructed [Tanigaki et al. (2006); Planche et al. (2009)] using either distributed, individually-
 477 powered coils on a flat pole piece or using a conventional gap-shaping technique. For the LhARA FFA, we
 478 propose a variation of the coil-dominated design recently proposed at the Rutherford Appleton Laboratory
 479 in R&D studies for the upgrade of the ISIS neutron and muon source. In this case, the nominal scaling field
 480 is achieved using a distribution of single-powered windings on a flat pole piece. The parameter k can then
 481 be tuned using up to three additional independently-powered windings. The extent of the fringe field across
 482 the radius of the magnet must be carefully controlled using a ‘field clamp’ to achieve zero chromaticity.
 483 An active clamp, in which additional windings are placed around one end of the magnet, may be used to
 484 control the flutter function and thereby vary independently the vertical tune of the FFA ring. The FFA is
 485 required to deliver beams over a range of energy; each energy requiring a particular setting for the ring
 486 magnets. Therefore, a laminated magnet design may be required to reduce the time needed to change the
 487 field. The magnet gap of 4.7 cm given in table 2 is estimated assuming a flat-pole design for the magnet.

488

489 3.4.3 Extraction Line

490 Substantial margins in the beam parameters were assumed in the design of the extraction line from the FFA
 491 due to uncertainties in the beam distributions originating from the Stage 1 beam transport, the FFA injection
 492 line, and potential distortions introduced by the presence of space-charge effects during acceleration in the
 493 ring. The beam emittance was therefore allowed to be as large as a factor of ten greater than the nominal
 494 value, which was derived by assuming that the normalised emittance is conserved from the source, through
 495 the Stage 1 beam line, and in the FFA ring. In the nominal case, the physical emittance of the beam is
 496 affected by adiabatic damping only. Substantial flexibility in the optics of the extraction line is required, as
 497 the extraction line must accommodate a wide spectrum of beam conditions to serve the *in vitro* and *in vivo*
 498 end-stations.

499 Detailed studies were carried out for proton beams with kinetic energies of 40 MeV and 127 MeV. Table
 500 4 gives the Twiss β values for different beam sizes for the 40 MeV and 127 MeV proton-beam energies
 501 assuming a Gaussian beam distribution. The optics and geometric acceptance of the system is approximately
 502 the same for the 40 MeV and 127 MeV beams, justifying the working hypothesis that beam emittance is
 503 approximately the same for both beam energies. This assumption will be revised as soon as space-charge
 504 simulations for the entire system are available.

505 The first two dipoles and four quadrupoles of the extraction line bend the beam coming from the extraction
 506 septum of the FFA such that it is parallel to the low-energy beam line while ensuring that dispersion is

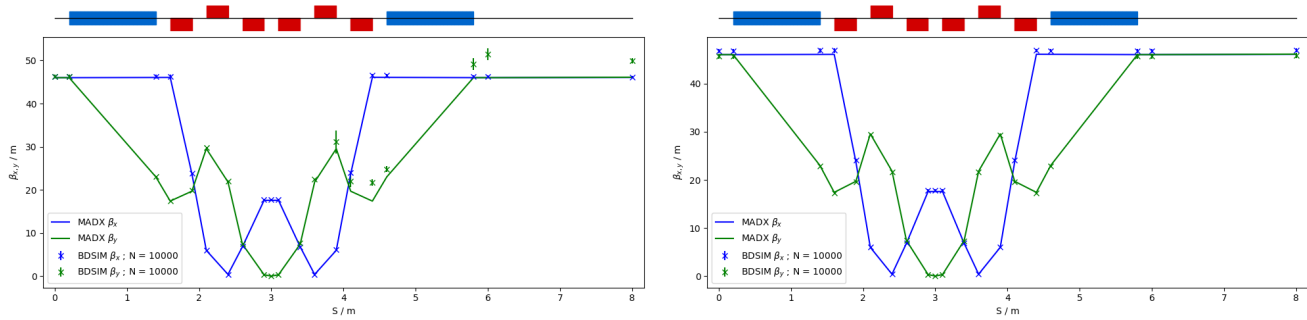


Figure 9. Comparison of MADX and BDSIM simulation of 40 MeV (left) and nominal 127 MeV (right) proton beam passing through the high energy *in vitro* arc simulated with 10^4 particles (in BDSIM).

507 closed. Closing the dispersion is critical, as off-momentum particles will follow trajectories different to
 508 those followed by particles with the design momentum and therefore impact the size and shape of the beam
 509 downstream. The second part of the extraction line consists of four quadrupoles which transport the beam
 510 either to the first dipole of the vertical arc that serves the high-energy *in vitro* end station or to the *in vivo*
 511 end station if this dipole is not energised. These quadrupoles provide the flexibility required to produce the
 512 different beam sizes for the *in vitro* end station, as specified in table 4.

513

514 3.4.4 High-energy *in vitro* beam line

515 The high-energy *in vitro* beam line transports the beam from the extraction line to the high-energy *in*
 516 *vitro* end station. The 90° vertical bend is a scaled version of the low-energy vertical arc, following the
 517 same design principles, and also consists of two bending dipole magnets and six quadrupole magnets. To
 518 accommodate the higher beam energies, the lengths of the magnets were scaled in order to ensure that
 519 peak magnetic fields were below the saturation limits of normal conducting magnets. The bending dipole
 520 magnet lengths were increased to 1.2 m each and the quadrupole lengths were tripled to 0.3 m. The overall
 521 length of the arc then becomes 6 m, compared to 4.6 m for the low energy *in vitro* arc. This difference in
 522 arc length means the high-energy *in vitro* arc finishes about 0.9 m higher than the low-energy one. This
 523 difference can easily be accommodated by adjusting the final drift lengths.

524 The quadrupole strengths for the scaled high-energy *in vitro* arc were obtained using MADX calculations,
 525 tracking simulations using BDSIM show good agreement with these, see figure 9. The input beam
 526 distribution used in BDSIM was assumed to be Gaussian with Twiss $\beta = 46$, which gives a beam size
 527 of about 10 mm. Small deviations from the BDSIM results were observed in GPT simulations due to
 528 space-charge effects.

529

530 3.4.5 *In vivo* beam line

531 To facilitate efficient small-animal handling, the end station dedicated to *in vivo* experiments will be
 532 positioned adjacent to the principle road access to the facility. If the first dipole of the high-energy *in vitro*
 533 arc is not energised, the beam is sent to the *in vivo* end station. From the end of the extraction line, 7.7 m of
 534 drift is necessary to clear the first bending dipole of the *in vitro* arc, to provide space for the five RF cavities
 535 needed for longitudinal phase-space manipulation and to allow space for diagnostic devices. Following this
 536 drift is a further 6.6 m of beam line that includes four quadrupoles, each of length 0.4 m, which are used to
 537 perform the final focusing adjustments of the beam delivered to the *in vivo* end station. A final 1.5 m drift
 538 length is reserved for scanning magnets so spot scanning can be performed and to allow for penetration of
 539 the shielding of the *in vivo* end station. In total, the *in vivo* beam line is 15.6 m in length.

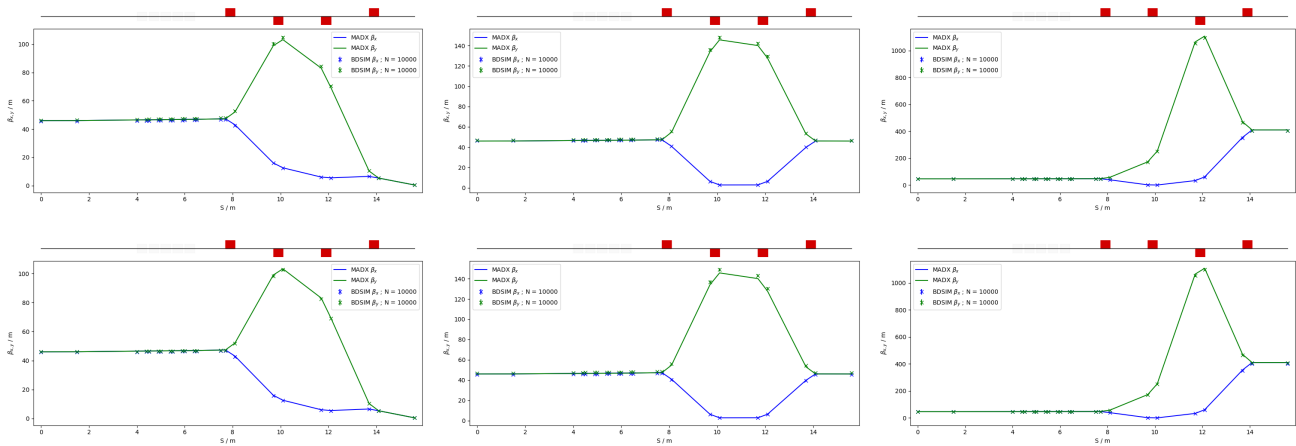


Figure 10. MADX and BDSIM simulations of the *in vivo* beam line for a 40 MeV proton beam (top row) and a nominal 127 MeV proton beam (bottom row) with quadrupoles matched to $\beta_{x,y} = 0.46$ m (left), $\beta_{x,y} = 46$ m (middle) and $\beta_{x,y} = 410$ m (right) for 10^4 particles.

540 The flexible design can match the various $\beta_{x,y}$ values given in table 4, but not the smallest target value of
 541 $\beta_{x,y} = 0.039$ m for the pessimistic scenario, which is very challenging. To verify that the optics design can
 542 provide the required beam sizes, simulations were performed with BDSIM using an input Gaussian beam
 543 generated with the Twiss β values given in tables 4. Figure 10 shows the results for a 40 MeV proton beam
 544 and a nominal emittance 127 MeV proton beam matched in order to obtain beam sizes of 1 mm, 10 mm
 545 and 30 mm.

546

547 3.5 Instrumentation

548 Commercial off-the-shelf (COTS) instrumentation will be used for Stages 1 and 2 of LhARA wherever
 549 possible. However, the characteristics of the beam (e.g. very high charge-per-bunch, low-to-moderate
 550 energy) will require that some custom solutions be developed. The authors are developing two concepts,
 551 termed SciWire and SmartPhantom, for the low- and high-energy *in vitro* end stations, respectively. These
 552 detectors can also be used for beam diagnostics and may find application at other facilities. Instrumentation
 553 for the detection of secondary particles arising from the interaction of the beam with tissue is not discussed
 554 here but is an important area that will be studied in the future.

555

556 3.5.1 SciWire

557 For the Stage 1 beam, the maximum proton energy is 15 MeV. Shot-to-shot characterisation of the beam is
 558 essential and requires the use of a very thin detector with a fast response. The SciWire [Kurup (2019)] is
 559 being developed to provide energy and intensity profile measurements for low-energy ion beams. A single
 560 SciWire plane consists of two layers of $250 \mu\text{m}$ square-section scintillating fibres, with the fibre directions
 561 in the two layers orthogonal to each other. A series of back-to-back planes provides a homogeneous volume
 562 of scintillator. If there are enough planes to stop the beam, the depth of penetration will allow the beam
 563 energy to be inferred. This is a destructive measurement so would only be performed when experiments are
 564 not running. A single plane, however, can be used for 2D beam-profile measurements while the beam is
 565 being delivered for experiments. Light from the SciWire fibres may be detected using a CMOS camera or
 566 photodiodes. If the instrumentation is sufficiently fast, the SciWire can be used to derive feedback signals
 567 for beam tuning.

568

569 3.5.2 SmartPhantom

570 To study the dose profile of Stage 2 beams in real time, the SmartPhantom [Barber (2018)] is being
571 developed. This is a water-filled phantom, instrumented with planes of scintillating fibres, used to infer
572 the dose distribution with distance. The detection elements of the SmartPhantom are 250 μm diameter,
573 round scintillating fibres. Each fibre station consists of two planes of fibres, in which the fibre directions
574 are orthogonal. Five fibre stations are arranged in the phantom in front of the cell-culture flask. The fibres
575 may be coupled to photodiodes, or a CMOS camera. Simulations in GEANT4 are being used to develop
576 analysis techniques to determine the position of the Bragg peak shot-by-shot. The beam profile and dose
577 delivered can then be calculated in real time.

578

579 3.5.3 Beam line Instrumentation

580 The requirement for instrumentation begins with the Ti:Sapphire laser. The laser focal spot will be
581 characterised using a camera-based system and high-speed wavefront measurements [Wang (2014)] from
582 COTS vendors.

583 For the Stage 1 beam line, beam position monitors (BPMs) will be needed for beam steering. Because
584 of the low beam energy, non-intercepting BPMs using capacitive pickup buttons will be used. Custom
585 pickups will be needed to match the beam pipe geometry, but COTS electronics are available. The beam
586 current will be monitored near the end of each beam line, using integrating current toroids (ICT), backed
587 up with the option of insertable multi-layer Faraday cups (MLFC) to give absolute beam current and energy
588 measurements. Beam profiles could be measured by SEM grids on both Stage 1 and Stage 2 beam lines.
589 For Stage 1, these monitors will be mounted on pneumatic actuators to avoid scattering. Each end station
590 could be equipped with insertable “pepper-pot” emittance monitors and a transverse deflection cavity with
591 fluorescent screen could be provided for bunch shape measurements.

592 The BPMs on the FFA will require pickup designs suitable for the unusual, wide and shallow vacuum
593 vessel. The FFA at the KURNS facility in Kyoto has a similar layout [Uesugi (2018)] and uses a kicker and
594 capacitive pickup to perform tune measurements in each transverse direction. A minimum of one BPM
595 every second cell will be used in the FFA so that the beam orbit can be measured. BPMs will also be
596 required close to the injection and extraction septa. The BPM system may be able to use COTS electronics,
597 but the pickups will be based on the KURNS design of multiple electrodes arranged across the vacuum
598 vessel width.

599 The data acquisition system needs to be able to store calibration data and apply corrections in real time. It
600 is necessary to be able to find the beam centre from a profile, even when the profile may be non-Gaussian
601 and possibly asymmetric. Field programmable gate arrays (FPGAs) can be used to perform fast fitting and
602 pattern recognition of beam profiles. The instrumentation will be integrated with the accelerator control
603 system and will provide fast feedback and adjustment of the beam parameters in real time.

604

605 3.6 Biological end stations

606 In order to deliver a successful radiobiological research programme, high-end and fully equipped *in vitro*
607 and *in vivo* end-stations will be housed within the LhARA facility. The two *in vitro* end-stations (high
608 and low energy) will contain vertically-delivered beam lines which will be used for the irradiation of 2D
609 monolayer and 3D-cell systems (spheroids and patient-derived organoids) in culture. The beam line within
610 the end-stations will be housed in sealed units that will be directly sourced with appropriate gases (carbon
611 dioxide and nitrogen), allowing for the cells within culture plates to be incubated for a short time in stable
612 conditions prior to and during irradiation. This will also enable the chamber to act, where necessary, as a

613 hypoxia unit (0.1%–5% oxygen concentration). Furthermore, these sealed units will contain robotics to
614 enable the numerous cell culture plates housed within to be placed into and taken out of the beam.

615 The *in vitro* end-stations will be located within a research laboratory equipped with state-of-the-art
616 facilities. The laboratory will include all the necessary equipment for bench-top science, sample processing
617 and analysis (e.g. refrigerated centrifuges and light/fluorescent microscopes), along with the equipment
618 required for contaminant-free cell culture (e.g. humidified CO₂ cell culture incubators, Class II biological
619 safety cabinets), and for the storage of biological samples and specimens (e.g. –20°C and –80°C freezers
620 and fridges). The laboratory will also house an X-ray irradiator (allowing direct RBE comparisons between
621 conventional photon irradiation, and the proton and carbon ions delivered by the accelerator), a hypoxia
622 chamber (for long-term hypoxia studies), a robotic workstation (for handling and processing of large sample
623 numbers, aiding high-throughput screening experiments), and an ultra-pure-water delivery system. These
624 facilities will enable a myriad of biological end-points to be investigated in both normal- and tumour-cell
625 models not only from routine clonogenic survival and growth assays, but also from significantly more
626 complex end-points (e.g. inflammation, angiogenesis, senescence and autophagy).

627 The *in vivo* end-station will be served with high-energy proton and carbon ions capable of penetrating
628 deeper into tissues allowing the irradiation of whole animals. The ability to perform *in vivo* pre-clinical
629 studies is vital for the future effective translation of the research into human cancer patients where optimum
630 treatment strategies and the reduction of side-effects are crucial. The *in vivo* end-station will allow the
631 irradiation of a number of small-animal models (e.g. xenograft mouse and rat models) which can further
632 promote an examination of particular ions on the appropriate biological end-points (e.g. tumour growth
633 and normal tissue responses). The end-station will contain a small-animal handling area which will allow
634 for the anaesthetisation of animals prior to irradiation. To enable the irradiation of small target volumes
635 with a high level of precision and accuracy, an image guidance system (e.g. computed tomography) will be
636 available. The animals will subsequently be placed in temperature-controlled holder tubes enabling the
637 correct positioning of the relevant irradiation area in front of the beam line. The beam size is sufficient to
638 give flexibility in the different irradiation conditions, in particular through passive scattering, pencil-beam
639 scanning, and micro-beam irradiation, to be investigated at both conventional and FLASH dose rates. It is
640 envisaged that the animals will be taken off-site post-irradiation to a nearby animal-holding facility for a
641 follow-up period where biological measurements will be conducted.

642

643 **3.7 Infrastructure and integration**

644 The LhARA facility will encompass two floors of roughly 42 m in length and 18 m wide. The ground floor
645 will contain the laser, accelerator, and *in vivo* end station while the first floor will house the laboratory area
646 and the two *in vitro* end stations. The entire facility will require radiation protection in the form of concrete
647 shielding. There will be three principal areas: a radiation controlled-access area, a laser controlled-access
648 area, and a laboratory limited-access area.

649 For a facility such as LhARA, laser, radiation and biological safety are primary concerns. It is envisaged
650 that LhARA will be built at a national laboratory or equivalent research institute which has an established
651 safety-management system and culture in place.

652 The infrastructure and integration of the LhARA facility will require R&D in four key areas: risk analysis
653 (project risks), risk assessments (safety risks), radiation simulations, and controls development. The risk
654 analysis will cover all aspects of the facility, such as funding and resource availability, not just technical
655 risks. A safety-risk assessment will be performed to describe and control all potential safety risks in the

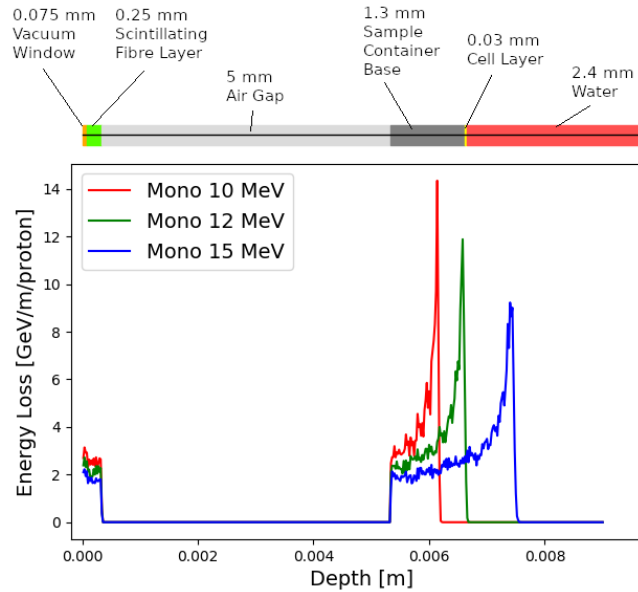


Figure 11. Energy loss as a function of depth in the low-energy *in vitro* end station for three monoenergetic proton energies: 10 MeV; 12 MeV; and 15 MeV. Each beam was simulated using 10^4 particles at the start of the end station. The material through which the beam passes is indicated above the figure. The entrance window is plotted at a Depth value of 0 m. The beam deposits energy in the beam window and the layer of scintillating fibre before passing through an air gap and entering the sample container.

656 facility. The safety-risk assessment will, to a reasonable degree, identify all pieces of equipment that
 657 require safety mitigations and identify control measures that must be put in place. Coupled closely with the
 658 safety-risk assessment, radiation simulations will be developed to characterise the radiation hazards in and
 659 around the LhARA facility. The last area to require R&D will be the control systems. It is expected that the
 660 facility will use the Experimental Physics and Industrial Control System [The EPICS collaboration (2020)],
 661 which can be further developed at this stage.

662

4 PERFORMANCE

663 The dose distributions delivered to the end stations were evaluated using BDSIM. Figure 11 shows the
 664 energy lost by the beam as it enters the low-energy *in vitro* end station. The beam passes through the
 665 vacuum window, a layer of scintillating fibre, and a 5 mm air gap. The beam then enters the cell-sample
 666 container, assumed to be polystyrene, which supports a $30\ \mu\text{m}$ thick layer of cells, modelled using the
 667 GEANT4 material “G4_SKIN_ICRP” [NIST (2017)]. The transverse momentum of protons in the beam
 668 was assumed to follow a Gaussian distribution, with a lateral spread small enough for the beam to be fully
 669 contained within the required spot size of 3 cm. Figure 11 shows that a proton beam with 10 MeV kinetic
 670 energy does not reach the cell layer. The Bragg peak of a 12 MeV proton beam is located close to the cell
 671 layer, while a 15 MeV beam, the maximum energy specified for delivery to the low-energy *in vitro* end
 672 station, has a Bragg peak located beyond the cell layer. LhARA’s ability to deliver various beam energies
 673 will allow the investigation of the radiobiological effects of irradiation using different parts of the Bragg
 674 peak, effectively varying the LET across the sample. RF cavities are placed in both the stage 1 and the
 675 stage 2 beam lines to allow the manipulation of the energy of the bunch as a function of time. This facility
 676 will allow the study of the impact of a “spread-out Bragg peak” (SOBP).

677 The maximum dose that can be delivered was evaluated for a variety of beam energies. In order for the
678 dose to be reported in units of Gray it is necessary to define the volume within which the energy deposition
679 is to be integrated. Therefore, the dose was estimated from simulations by calculating the energy deposited
680 in a volume of water corresponding in size to the sensitive volume of a PTW 23343 Markus ion chamber
681 [PTW (2019/2020)] placed at the position of the Bragg peak in each case. This choice allows the doses and
682 dose-rates reported here to be compared to those of operating facilities. The cylindrical sensitive volume of
683 the ion chamber has a radius of 2.65 mm and a depth of 2 mm, giving a volume of about $4.4 \times 10^{-8} \text{ m}^3$.
684 The total energy deposited within the chamber was recorded and converted into dose in units of Gray.

685 For the low-energy *in vitro* end station, the minimum spot size has a diameter of 10 mm, which is
686 larger than the area of the chamber. A single shot of 10^9 protons at 12 MeV with this spot size deposits
687 $3.1 \times 10^{-4} \text{ J}$ in the chamber volume, corresponding to a dose of 7.1 Gy. For this simulation, the thickness
688 of the sample container was reduced so that the Bragg peak could be positioned within the chamber volume.
689 For the bunch length of 7.0 ns, the maximum instantaneous dose rate is $1.0 \times 10^9 \text{ Gy/s}$ and the average
690 dose rate is 71 Gy/s, assuming a repetition rate of 10 Hz. A single shot of 10^9 protons at 15 MeV deposits
691 $5.6 \times 10^{-4} \text{ J}$ in the chamber volume, corresponding to a dose of 12.8 Gy. This gives an instantaneous dose
692 rate of $1.8 \times 10^9 \text{ Gy/s}$ and an average dose rate of 128 Gy/s assuming the same bunch length and repetition
693 rate as for the 12 MeV case.

694 For the high-energy *in vitro* end station, a similar design to the low-energy end station was used, but the
695 air gap was increased from 5 mm to 5 cm and a water phantom was placed at the end of the air gap instead
696 of a cell culture plate. The water phantom used in the simulation was based upon the PTC T41023 water
697 phantom [PTW (2009)]. In addition, the smaller minimum design beam size of 1 mm was used. A single
698 shot of 10^9 protons at 127 MeV deposits $6.9 \times 10^{-4} \text{ J}$ in the chamber at the pristine Bragg peak depth,
699 corresponding to a dose of 15.6 Gy, an instantaneous dose rate of $3.8 \times 10^8 \text{ Gy/s}$ and an average dose rate
700 of 156 Gy/s. The end-station design assumed for a 33.4 MeV/u carbon beam was the same as that used for
701 the low-energy *in vitro* end station due to the limited range in water of the carbon beam. The intensity of the
702 beam is a factor of 12 less than that for protons in order to preserve the same strength of the space-charge
703 effect at injection into the FFA with the same beam parameters, as the incoherent space charge tune shift is
704 proportional to q^2/A and inversely proportional to $\beta^2\gamma^3$, where q is the particle charge, A its mass number,
705 and β and γ its relativistic parameters. A single pulse of 8.3×10^7 ions deposits $3.2 \times 10^{-3} \text{ J}$ at the depth
706 of the pristine Bragg peak, leading to an instantaneous dose rate of $9.7 \times 10^8 \text{ Gy/s}$ and a maximum average
707 dose rate of 730 Gy/s.

708 The expected maximum dose rates are summarised in table 5. The instantaneous dose rates depend on the
709 bunch length which differs depending on the energies. For the low-energy *in vitro* line, a 7 ns bunch length
710 is assumed for all energies. For the higher energies, a 127 MeV proton beam is delivered with a bunch
711 length of 41.5 ns, and a bunch length of 75.2 ns for a 33.4 MeV/u carbon beam. The same repetition rate of
712 10 Hz was used for all energies. The minimum beam size at the start of the end station for the 12 MeV and
713 15 MeV proton-beam simulations was 1 cm. A 1 mm beam size was used for the 127 MeV proton beam and
714 33.4 MeV/u carbon-ion beam simulations.

715

5 CONCLUSIONS

716 The initial conceptual design of LhARA, the Laser-hybrid Accelerator for Radiobiological Applications,
717 has been described and its performance evaluated in simulations that take into account the key features
718 of the facility. LhARA uses a laser-driven source to create a large flux of protons or light ions which are

Table 5. Summary of expected maximum dose per pulse and dose rates that LhARA can deliver for minimum beam sizes. These estimates are based on Monte Carlo simulations using a bunch length of 7 ns for 12 MeV and 15 MeV proton beams, 41.5 ns for the 127 MeV proton beam and 75.2 ns for the 33.4 MeV/u carbon beam. The average dose rate is based on the 10 Hz repetition rate of the laser source.

	12 MeV Protons	15 MeV Protons	127 MeV Protons	33.4 MeV/u Carbon
Dose per pulse	7.1 Gy	12.8 Gy	15.6 Gy	73.0 Gy
Instantaneous dose rate	1.0×10^9 Gy/s	1.8×10^9 Gy/s	3.8×10^8 Gy/s	9.7×10^8 Gy/s
Average dose rate	71 Gy/s	128 Gy/s	156 Gy/s	730 Gy/s

719 captured and formed into a beam by strong-focusing plasma lenses, thus evading prevalent space-charge
 720 limits on the instantaneous dose rate that can be delivered. Acceleration, performed using a fixed-field
 721 alternating-gradient accelerator, preserves the unique flexibility in the time, spectral, and spatial structure
 722 of the beam afforded by the laser-driven source. The ability to trigger the laser pulse that initiates the
 723 production of protons or ions at LhARA will allow the time structure of the beam to be varied to interrupt the
 724 chemical and biological pathways that determine the biological response to ionising radiation. The almost
 725 parallel beam that LhARA will deliver can be varied to illuminate a circular area with a maximum diameter
 726 of between 1 cm and 3 cm with an almost uniform dose, or focused to a spot with diameter of ~ 1 mm.
 727 These features will allow radiobiological studies to be carried out in completely new regimens, delivering a
 728 variety of ion species in a broad range of time structures and spatial configurations at instantaneous dose
 729 rates up to and potentially significantly beyond the current ultra-high dose-rate “FLASH” regime.

730 The enhanced understanding these studies will provide, may in turn result in new approaches to
 731 radiotherapy, decreasing the radio-toxicity for normal tissue while maintaining or enhancing the tumour-
 732 control probability. Further, by developing a triggerable system that incorporates dose-deposition imaging
 733 in a fast feedback-and-control system, in the long term LhARA has the potential to remove the requirement
 734 for a large gantry for proton and ion therapy, laying the foundations for “best in class” treatments to be
 735 made available to the many by reducing the footprint of future particle-beam therapy systems.

736 The radiobiology programme in combination with the demonstration in operation of the laser-hybrid
 737 technique means that the LhARA programme has the potential to drive a step-change in the clinical practice
 738 of proton- and ion-beam therapy.

739

ACKNOWLEDGEMENTS

740 The work described here was made possible by a grant from the Science and Technology Facilities Council
 741 (ST/T002638/1, ST/P002021/1). Additional support was provided by the STFC Rutherford Appleton and
 742 Daresbury Laboratories and members of the LhARA consortium. We gratefully acknowledge all sources
 743 of support. A pre-publication review of the pre-CDR for LhARA was carried out by P. Bolton (LMU,
 744 Munich), M. Lamont (CERN), Y. Prezado (Institut Curie), and F. Romano (INFN-LNS and the National
 745 Physical Laboratory). We are grateful to the review panel for their support and detailed feedback on the
 746 draft pre-CDR.

747

REFERENCES

- 748 (2009). *User Manual Water Phantom T41023*. PTW-Freiburg Physikalisch-Technische Werkstätten Dr.
749 Pychlau GmbH, d738.131.00/02 en edn.
- 750 (2019/2020). *Ionizing Radiation Detectors*. PTW-Freiburg Physikalisch-Technische Werkstätten Dr.
751 Pychlau GmbH
- 752 [Dataset] (2020). Vsim for plasma. <https://www.txcorp.com/vsim>
- 753 [Dataset] A-SAIL Project (2020). A-sail project. [https://www.qub.ac.uk/
754 research-centres/A-SAILProject/](https://www.qub.ac.uk/research-centres/A-SAILProject/)
- 755 Amin, T., Barlow, R., Ghithan, S., Royb, G., and Schuhb, S. (2018). Formation of a uniform ion beam
756 using octupole magnets for bioleir facility at cern. *JINST* 13, P04016
- 757 Atun, R., Jaffray, D. A., Barton, M. B., Bray, F., Baumann, M., Vikram, B., et al. (2015). Expanding
758 global access to radiotherapy. *The Lancet Oncology* 16, 1153 – 1186. doi:[https://doi.org/10.1016/
759 S1470-2045\(15\)00222-3](https://doi.org/10.1016/S1470-2045(15)00222-3)
- 760 Autin, B., Carli, C., D’Amico, T., Gröbner, O., Martini, M., and Wildner, E. (1998). *BeamOptics:*
761 *A program for analytical beam optics*. Tech. Rep. CERN–98-06, European Organization for
762 Nuclear Research (CERN). [http://inis.iaea.org/search/search.aspx?orig_q=RN:
763 30052986](http://inis.iaea.org/search/search.aspx?orig_q=RN:30052986)
- 764 Barber, G. (2018). Outline design and cost estimate for the SmartPhantom. *Unpublished note*
- 765 Berry, R. J. (1973). EFFECTS OF RADIATION DOSE-RATE: From Protracted, Continuous Irradiation
766 to Ultra-High Dose-Rates from Pulsed Accelerators. *British Medical Bulletin* 29, 44–47. doi:10.1093/
767 oxfordjournals.bmb.a070955
- 768 Bin, J., Allinger, K., Assmann, W., Dollinger, G., Drexler, G. A., Friedl, A. A., et al. (2012). A laser-
769 driven nanosecond proton source for radiobiological studies. *Applied Physics Letters* 101, 243701.
770 doi:10.1063/1.4769372
- 771 Bin, J., Ma, W., Wang, H., Streeter, M., Kreuzer, C., Kiefer, D., et al. (2015). Ion Acceleration Using
772 Relativistic Pulse Shaping in Near-Critical-Density Plasmas. *Physical Review Letters* 115, 064801.
773 doi:10.1103/PhysRevLett.115.064801
- 774 Bourhis, J., WJ, S., PG, J., O, G., C, B., F, D., et al. (2019). Treatment of a first patient with FLASH-
775 radiotherapy. *Radiotherapy and oncology : journal of the European Society for Therapeutic Radiology
776 and Oncology* 139. doi:10.1016/J.RADONC.2019.06.019
- 777 Bray, F., Ferlay, J., Soerjomataram, I., Siegel, R. L., Torre, L. A., and Jemal, A. (2018). Global cancer
778 statistics 2018: GLOBOCAN estimates of incidence and mortality worldwide for 36 cancers in 185
779 countries. *CA: A Cancer Journal for Clinicians* 68, 394–424. doi:10.3322/caac.21492
- 780 Bulanov, S., Esirkepov, T., Khoroshkov, V., Kuznetsov, A., and Pegoraro, F. (2002). Oncological
781 hadrontherapy with laser ion accelerators. *Physics Letters A* 299, 240–247. doi:[https://doi.org/10.1016/
782 S0375-9601\(02\)00521-2](https://doi.org/10.1016/S0375-9601(02)00521-2)
- 783 Carter, R. J., Nickson, C. M., Thompson, J. M., Kacperek, A., Hill, M. A., and Parsons, J. L. (2018).
784 Complex dna damage induced by high linear energy transfer alpha-particles and protons triggers a
785 specific cellular dna damage response. *International Journal of Radiation Oncology*Biophysics*Physics*
786 100, 776 – 784. doi:<https://doi.org/10.1016/j.ijrobp.2017.11.012>
- 787 Chaudhary, P., Gwynne, D., Doria, D., Romagnani, L., Maiorino, C., Padda, H., et al. (2017). Effectiveness
788 of laser accelerated ultra high dose rate protons in DNA DSB damage induction under hypoxic conditions.
789 In *44th EPS Conference on Plasma Physics, EPS 2017* (European Physical Society (EPS)), vol. 44F.
790 P1.217

- 791 Chaudhary, P., Marshall, T. I., Perozziello, F. M., Manti, L., Currell, F. J., Hanton, F., et al. (2014). Relative
792 Biological Effectiveness Variation Along Monoenergetic and Modulated Bragg Peaks of a 62-MeV
793 Therapeutic Proton Beam: A Preclinical Assessment. *International Journal of Radiation Oncology •*
794 *Biology • Physics* 90, 27–35. doi:10.1016/j.ijrobp.2014.05.010
- 795 Chen, S. N., Vranic, M., Gangolf, T., Boella, E., Antici, P., Bailly-Grandvaux, M., et al. (2017). Collimated
796 protons accelerated from an overdense gas jet irradiated by a 1 μm wavelength high-intensity short-pulse
797 laser. *Scientific Reports* 7, 13505. doi:10.1038/s41598-017-12910-6
- 798 Cirrone, G., Catalano, R., Cuttone, G., Margarone, D., Schillaci, F., and Petringa, G. (2020). Generation
799 control and application of flash radiation beam from laser-matter interaction: The ELIMAIA-ELIMED
800 beamline. *Nuovo Cim. C* 43, 15. doi:10.1393/ncc/i2020-20015-6
- 801 Cirrone, G. et al. (2016). Status, Plans and Potential Applications of the ELIMED Beam Line at
802 ELI-Beamlines. In *7th International Particle Accelerator Conference*. WEXB01. doi:10.18429/
803 JACoW-IPAC2016-WEXB01
- 804 Cirrone, G. A. P., Margarone, D., Maggiore, M., Anzalone, A., Borghesi, M., Jia, S. B., et al. (2013).
805 ELIMED: a new hadron therapy concept based on laser driven ion beams. In *Laser Acceleration of*
806 *Electrons, Protons, and Ions II; and Medical Applications of Laser-Generated Beams of Particles II;*
807 *and Harnessing Relativistic Plasma Waves III*, eds. E. Esarey, C. B. Schroeder, W. P. Leemans, K. W. D.
808 Ledingham, and D. A. Jaroszynski. International Society for Optics and Photonics (SPIE), vol. 8779,
809 216 – 225. doi:10.1117/12.2026530
- 810 Clark, E. L., Krushelnick, K., Davies, J. R., Zepf, M., Tatarakis, M., Beg, F. N., et al. (2000a).
811 Measurements of energetic proton transport through magnetized plasma from intense laser interactions
812 with solids. *Phys. Rev. Lett.* 84, 670–673. doi:10.1103/PhysRevLett.84.670
- 813 Clark, E. L., Krushelnick, K., Zepf, M., Beg, F. N., Tatarakis, M., Machacek, A., et al. (2000b). Energetic
814 heavy-ion and proton generation from ultraintense laser-plasma interactions with solids. *Phys. Rev. Lett.*
815 85, 1654–1657. doi:10.1103/PhysRevLett.85.1654
- 816 Daido, H., Nishiuchi, M., and Pirozhkov, A. S. (2012). Review of laser-driven ion sources and their
817 applications. *Reports on Progress in Physics* 75, 56401. doi:10.1088/0034-4885/75/5/056401
- 818 Datta, N. R., Rogers, S., and Bodis, S. (2019). Challenges and Opportunities to Realize “The 2030 Agenda
819 for Sustainable Development” by the United Nations: Implications for Radiation Therapy Infrastructure
820 in Low- and Middle-Income Countries. *International Journal of Radiation Oncology*Biography*Physics*
821 105, 918–933. doi:https://doi.org/10.1016/j.ijrobp.2019.04.033
- 822 De Loos, M. J. and Van der Geer, S. B. (1996). General Particle Tracer: A New 3D Code for Accelerator
823 and Beamline Design
- 824 deGrassie, J. S. and Malmberg, J. H. (1980). Waves and transport in the pure electron plasma. *The Physics*
825 *of Fluids* 23, 63–81. doi:10.1063/1.862864
- 826 Doria, D., Kakolee, K. F., Kar, S., Litt, S. K., Fiorini, F., Ahmed, H., et al. (2012). Biological effectiveness
827 on live cells of laser driven protons at dose rates exceeding 10^9 Gy/s. *AIP Advances* 2, 011209.
828 doi:10.1063/1.3699063
- 829 Dover, N., Nishiuchi, M., Sakaki, H., Kondo, K., Lowe, H., Alkhimova, M., et al. (2020). Demonstration
830 of repetitive energetic proton generation by ultra-intense laser interaction with a tape target. *High Energy*
831 *Density Physics* 37, 100847. doi:10.1016/j.hedp.2020.100847
- 832 Durante, M., Bräuer-Krisch, E., and Hill, M. (2018). Faster and safer? flash ultra-high dose rate in
833 radiotherapy. *The British Journal of Radiology* 91, 20170628. doi:10.1259/bjr.20170628. PMID:
834 29172684

- 835 Favaudon, V., Caplier, L., Monceau, V., Pouzoulet, F., Sayarath, M., Fouillade, C., et al. (2014). Ultrahigh
836 dose-rate flash irradiation increases the differential response between normal and tumor tissue in mice.
837 *Science Translational Medicine* 6, 245ra93–245ra93. doi:10.1126/scitranslmed.3008973
- 838 Fiorini, F., Kirby, D., Borghesi, M., Doria, D., Jeynes, J. C., Kakolee, K. F., et al. (2011). Dosimetry and
839 spectral analysis of a radiobiological experiment using laser-driven proton beams. *Phys Med Biol* 56,
840 6969–6982
- 841 Fitzmaurice, C., Akinyemiju, T. F., Al Lami, F. H., Alam, T., Alizadeh-Navaei, R., Allen, C., et al. (2018).
842 Global, Regional, and National Cancer Incidence, Mortality, Years of Life Lost, Years Lived With
843 Disability, and Disability-Adjusted Life-Years for 29 Cancer Groups, 1990 to 2016. *JAMA Oncology* 4,
844 1553. doi:10.1001/jamaoncol.2018.2706
- 845 Fourkal, E., Li, J. S., Ding, M., Tajima, T., and Ma, C. M. (2003). Particle selection for laser-accelerated
846 proton therapy feasibility study. *Medical Physics* 30, 1660–1670. doi:10.1118/1.1586268
- 847 Fourier, J., Martinache, F., Meot, F., and Pasternak, J. (2008). Spiral ffac lattice design tools. application
848 to 6-d tracking in a proton-therapy class lattice. *Nucl. Instrum. Meth. A* 589, 133–142. doi:10.1016/j.
849 nima.2008.01.082
- 850 Gabor, D. (1947). A Space-Charge Lens for the Focusing of Ion Beams. *Nature* 160, 89–90. doi:10.1038/
851 160089b0
- 852 Gauthier, M., Curry, C. B., Göde, S., Brack, F.-E., Kim, J. B., MacDonald, M. J., et al. (2017). High
853 repetition rate, multi-mev proton source from cryogenic hydrogen jets. *Applied Physics Letters* 111,
854 114102. doi:10.1063/1.4990487
- 855 González, W. and Prezado, Y. (2018). Spatial fractionation of the dose in heavy ions therapy: An
856 optimization study. *Medical Physics* 45, 2620–2627. doi:10.1002/mp.12902
- 857 Grote, H. and Schmidt, F. (2003). MAD-X: An upgrade from MAD8. *Conf. Proc. C* 030512, 3497
- 858 Karger, C. P. and Peschke, P. (2017). RBE and related modeling in carbon-ion therapy. *Physics in Medicine
859 & Biology* 63, 01TR02. doi:10.1088/1361-6560/aa9102
- 860 Kraft, S. D., Richter, C., Zeil, K., Baumann, M., Beyreuther, E., Bock, S., et al. (2010). Dose-dependent
861 biological damage of tumour cells by laser-accelerated proton beams. *New Journal of Physics* 12, 85003.
862 doi:10.1088/1367-2630/12/8/085003
- 863 Krest, D., Laslett, L., Jones, L. W., Symon, K., and Terwilliger, K. (1956). *Fixed field alternating gradient
864 particle accelerators*. Tech. Rep. MURA-109, MURA-DWK-KRS-LJL-LWJ-KMT-3, Midwestern
865 Universities Research Association (MURA)
- 866 Kurup, A. (2019). Diagnostics for LhARA. *Low energy ion beam diagnostics workshop, Imperial College*
- 867 Lagrange, J. B., Appleby, R. B., Garland, J. M., Pasternak, J., and Tygier, S. (2018). Racetrack FFAG
868 muon decay ring for nuSTORM with triplet focusing. *JINST* 13, P09013. doi:10.1088/1748-0221/13/
869 09/P09013
- 870 Loeffler, J. S. and Durante, M. (2013). Charged particle therapy—optimization, challenges and future
871 directions. *Nature Reviews Clinical Oncology* 10, 411–424. doi:10.1038/nrclinonc.2013.79
- 872 Malka, V., Fritzler, S., Lefebvre, E., d’Humières, E., Ferrand, R., Grillon, G., et al. (2004). Practicability of
873 proton therapy using compact laser systems. *Medical Physics* 31, 1587–1592. doi:10.1118/1.1747751
- 874 Malmberg, J. H., Driscoll, C. F., Beck, B., Eggleston, D. L., Fajans, J., Fine, K., et al. (1988). Experiments
875 with pure electron plasmas. *AIP Conference Proceedings* 175, 28–74. doi:10.1063/1.37613
- 876 Manti, L., Perozziello, F. M., Borghesi, M., Candiano, G., Chaudhary, P., Cirrone, G. A., et al. (2017).
877 The radiobiology of laser-driven particle beams: Focus on sub-lethal responses of normal human cells.
878 *Journal of Instrumentation* 12. doi:10.1088/1748-0221/12/03/C03084

- 879 Margarone, D., Cirrone, G. A. P., Cuttone, G., Amico, A., Andò, L., Borghesi, M., et al. (2018).
880 Elimaia: A laser-driven ion accelerator for multidisciplinary applications. *Quantum Beam Science* 2,
881 doi:10.3390/qubs2020008
- 882 Margarone, D., Velyhan, A., Dostal, J., Ullschmied, J., Perin, J. P., Chatain, D., et al. (2016). Proton
883 acceleration driven by a nanosecond laser from a cryogenic thin solid-hydrogen ribbon. *Phys. Rev. X* 6,
884 041030. doi:10.1103/PhysRevX.6.041030
- 885 Martínez-Rovira, I., W, G., S, B., and Y, P. (2017). Carbon and oxygen minibeam radiation therapy: An
886 experimental dosimetric evaluation. *Medical physics* 44. doi:10.1002/MP.12383
- 887 Masood, U., Bussmann, M., Cowan, T. E., Enghardt, W., Karsch, L., Kroll, F., et al. (2014). A
888 compact solution for ion beam therapy with laser accelerated protons. *Applied Physics B* 117, 41–52.
889 doi:https://doi.org/10.1007/s00340-014-5796-z
- 890 Masood, U., Cowan, T. E., Enghardt, W., Hofmann, K. M., Karsch, L., Kroll, F., et al. (2017). A
891 light-weight compact proton gantry design with a novel dose delivery system for broad-energetic
892 laser-accelerated beams. *Physics in Medicine & Biology* 62, 5531–5555. doi:10.1088/1361-6560/aa7124
- 893 Meusel, O., Droba, M., Glaeser, B., and Schulte, K. (2013). Experimental studies of stable confined electron
894 clouds using Gabor lenses. *Conf. Proc. C* 1206051, 157–160. doi:10.5170/CERN-2013-002.157
- 895 Milluzzo, G. et al. (2017). Laser-accelerated ion beam diagnostics with TOF detectors for the ELIMED
896 beam line. *JINST* 12, C02025. doi:10.1088/1748-0221/12/02/C02025
- 897 Milluzzo, G. et al. (2018). Geant4 simulation of the ELIMED transport and dosimetry beam line for
898 high-energy laser-driven ion beam multidisciplinary applications. *Nucl. Instrum. Meth. A* 909, 298–302.
899 doi:10.1016/j.nima.2018.02.066
- 900 Morrison, J. T., Feister, S., Frische, K. D., Austin, D. R., Ngirmang, G. K., Murphy, N. R., et al. (2018).
901 MeV proton acceleration at kHz repetition rate from ultra-intense laser liquid interaction. *New Journal*
902 *of Physics* 20, 22001. doi:10.1088/1367-2630/aaa8d1
- 903 Nevay, L. J. et al. (2020). Bdsim: An accelerator tracking code with particle-matter interactions. *Computer*
904 *Physics Communications* , 107200
- 905 NIST (2017). *NIST Standard Reference Database 124* (National Institute of Standards and Technology).
906 doi:https://dx.doi.org/10.18434/T4NC7P
- 907 Noaman-ul Haq, M., Ahmed, H., Sokollik, T., Yu, L., Liu, Z., Yuan, X., et al. (2017). Statistical analysis of
908 laser driven protons using a high-repetition-rate tape drive target system. *Phys. Rev. Accel. Beams* 20,
909 041301. doi:10.1103/PhysRevAccelBeams.20.041301
- 910 Obst, L., Göde, S., Rehwald, M., Brack, F.-E., Branco, J., Bock, S., et al. (2017). Efficient laser-driven
911 proton acceleration from cylindrical and planar cryogenic hydrogen jets. *Scientific Reports* 7, 10248.
912 doi:10.1038/s41598-017-10589-3
- 913 Paganetti, H. (2014). Relative biological effectiveness (RBE) values for proton beam therapy. Variations as
914 a function of biological endpoint, dose, and linear energy transfer. *Phys. Med. Biol.* 59, R419
- 915 Paganetti, H. and van Luijk, P. (2013). Biological considerations when comparing proton therapy with
916 photon therapy. *Seminars in Radiation Oncology* 23, 77 – 87. doi:https://doi.org/10.1016/j.semradonc.
917 2012.11.002. Controversies in Proton Therapy
- 918 Passoni, M., Bertagna, L., and Zani, A. (2010). Target normal sheath acceleration: theory, comparison with
919 experiments and future perspectives. *New Journal of Physics* 12, 045012. doi:10.1088/1367-2630/12/4/
920 045012
- 921 Pipek, J. et al. (2017). Monte Carlo simulation of the ELIMED beamline using Geant4. *JINST* 12, C03027.
922 doi:10.1088/1748-0221/12/03/C03027

- 923 Planche, T., Fourrier, J., Lancelot, J. L., Meot, F., Neuveglise, D., and Pasternak, J. (2009). Design of a
924 prototype gap shaping spiral dipole for a variable energy protontherapy FFAG. *Nucl. Instrum. Meth.*
925 *A604*, 435–442. doi:10.1016/j.nima.2009.02.026
- 926 Pommarel, L., Vauzour, B., Mégnin-Chanet, F., Bayart, E., Delmas, O., Goudjil, F., et al. (2017). Spectral
927 and spatial shaping of a laser-produced ion beam for radiation-biology experiments. *Physical Review*
928 *Accelerators and Beams* 20, 1–10. doi:10.1103/PhysRevAccelBeams.20.032801
- 929 Pozimski, J. and Aslaninejad, M. (2013). Gabor lenses for capture and energy selection of laser driven ion
930 beams in cancer treatment. *Laser and Particle Beams* 31, 723–733. doi:10.1017/S0263034613000761
- 931 Prezado, Y., Dos Santos, M., Gonzalez, W., Jouvion, G., Guardiola, C., Heinrich, S., et al. (2017a). Transfer
932 of Minibeam Radiation Therapy into a cost-effective equipment for radiobiological studies: a proof of
933 concept. *Scientific Reports* 7, 17295. doi:10.1038/s41598-017-17543-3
- 934 Prezado, Y. and Fois, G. (2013). Proton-minibeam radiation therapy: a proof of concept. *Medical physics*
935 40. doi:10.1118/1.4791648
- 936 Prezado, Y., Jouvion, G., Hardy, D., Patriarca, A., Nauraye, C., Bergs, J., et al. (2017b). Proton minibeam
937 radiation therapy spares normal rat brain: Long-Term Clinical, Radiological and Histopathological
938 Analysis. *Scientific Reports* 7, 14403. doi:10.1038/s41598-017-14786-y
- 939 Prezado, Y., Jouvion, G., Patriarca, A., Nauraye, C., Guardiola, C., Juchaux, M., et al. (2018). Proton
940 minibeam radiation therapy widens the therapeutic index for high-grade gliomas. *Scientific Reports* 8.
941 doi:10.1038/s41598-018-34796-8
- 942 [Dataset] PTCOG (2020). Particle Therapy Co-Operative Group
- 943 Reiser, M. (1989). Comparison of gabor lens, gas focusing, and electrostatic quadrupole focusing for
944 low-energy ion beams. In *Proceedings of the 1989 IEEE Particle Accelerator Conference*, . 'Accelerator
945 *Science and Technology*. 1744–1747 vol.3
- 946 Romano, F., Schillaci, F., Cirrone, G., Cuttone, G., Scuderi, V., Allegra, L., et al. (2016a). The elimed
947 transport and dosimetry beamline for laser-driven ion beams. *Nuclear Instruments and Methods in*
948 *Physics Research Section A: Accelerators, Spectrometers, Detectors and Associated Equipment* 829,
949 153–158. doi:https://doi.org/10.1016/j.nima.2016.01.064. 2nd European Advanced Accelerator Concepts
950 Workshop – EAAC 2015
- 951 Romano, F. et al. (2016b). The ELIMED transport and dosimetry beamline for laser-driven ion beams.
952 *Nucl. Instrum. Meth. A* 829, 153–158. doi:10.1016/j.nima.2016.01.064
- 953 Schillaci, F. et al. (2019). Advanced Beam Transport Solutions for ELIMAIA: A User Oriented Laser-
954 Driven Ion Beamlines. In *10th International Particle Accelerator Conference*. TUPTS005. doi:10.
955 18429/JACoW-IPAC2019-TUPTS005
- 956 Snavely, R. A., Key, M. H., Hatchett, S. P., Cowan, T. E., Roth, M., Phillips, T. W., et al. (2000). Intense
957 high-energy proton beams from petawatt-laser irradiation of solids. *Phys. Rev. Lett.* 85, 2945–2948.
958 doi:10.1103/PhysRevLett.85.2945
- 959 Symon, K. R., Kerst, D. W., Jones, L. W., Laslett, L. J., and Terwilliger, K. M. (1956). Fixed-field
960 alternating-gradient particle accelerators. *Phys. Rev.* 103, 1837–1859. doi:10.1103/PhysRev.103.1837
- 961 Tanigaki, M., Mori, Y., Inoue, M., Mishima, K., Shiroya, S., Ishi, Y., et al. (2006). Present status of the
962 ffag accelerators in kurri for ads study. In *EPAC 2006 - Contributions to the Proceedings*
- 963 [Dataset] The EPICS collaboration (2020). The Experimental Physics and Industrial Control System.
964 <https://epics-controls.org>
- 965 The LhARA consortium (2020). *The Laser-hybrid Accelerator for Radiobiological Applications*.
966 Tech. Rep. CCAP-TN-01. [https://ccap.hep.ph.ic.ac.uk/trac/raw-attachment/
967 wiki/Research/DesignStudy/PreCDR/Review/2020-03-31-LhARA_pre_CDR-d2](https://ccap.hep.ph.ic.ac.uk/trac/raw-attachment/wiki/Research/DesignStudy/PreCDR/Review/2020-03-31-LhARA_pre_CDR-d2).

- 968 0.pdf
- 969 [Dataset] The World Health Organisation (2020). Cancer. [https://www.who.int/news-room/](https://www.who.int/news-room/fact-sheets/detail/cancer)
- 970 [fact-sheets/detail/cancer](https://www.who.int/news-room/fact-sheets/detail/cancer)
- 971 Thompson, R. C. (2015). PENNING TRAPS. In *Trapped Charged Particles* (WORLD SCIENTIFIC
- 972 (EUROPE)), Advanced Textbooks in Physics. 1–33. doi:10.1142/9781786340139_0001
- 973 Tsoupas, N. et al. (1991). Uniform beam distributions using octupoles. *Proceedings of PAC 1991*,
- 974 1695–1697
- 975 Uesugi, T. (2018). Betatron Tune Measurement. *FFA School, Osaka*
- 976 Urakabe, E. et al. (1999). Beam-profile control using an octupole magnet. *Jpn. J. Appl. Phys.* 38,
- 977 6145–6149
- 978 Vitti, E. T. and Parsons, J. L. (2019). The radiobiological effects of proton beam therapy: Impact on dna
- 979 damage and repair. *Cancers* 11. doi:10.3390/cancers11070946
- 980 Vozenin, M.-C., Hendry, J. H., and Limoli, C. L. (2019). Biological benefits of ultra-high dose rate flash
- 981 radiotherapy: Sleeping beauty awoken. *Clinical Oncology* 31, 407–415. doi:10.1016/j.clon.2019.04.001
- 982 Wang, H. (2014). Wavefront measurement techniques used in high power lasers. *High Power Laser Science*
- 983 *and Engineering* 2
- 984 Wiggins, S. M., Boyd, M., Brunetti, E., Butler, N. M. H., Feehan, J. S., Gray, R. J., et al. (2019). Application
- 985 programmes at the Scottish Centre for the Application of Plasma-based Accelerators (SCAPA). In
- 986 *Relativistic Plasma Waves and Particle Beams as Coherent and Incoherent Radiation Sources III*, eds.
- 987 D. A. Jaroszynski and M. Hur. International Society for Optics and Photonics (SPIE), vol. 11036, 93 –
- 988 103. doi:10.1117/12.2520717
- 989 Wilkens, J. J. and Oelfke, U. (2004). A phenomenological model for the relative biological effectiveness in
- 990 therapeutic proton beams. *Physics in Medicine and Biology* 49, 2811–2825. doi:10.1088/0031-9155/49/
- 991 13/004
- 992 Willingale, L., Nagel, S. R., Thomas, A. G. R., Bellei, C., Clarke, R. J., Dangor, A. E., et al. (2009).
- 993 Characterization of High-Intensity Laser Propagation in the Relativistic Transparent Regime through
- 994 Measurements of Energetic Proton Beams. *Physical Review Letters* 102, 125002. doi:10.1103/
- 995 PhysRevLett.102.125002
- 996 Wilson, J., Hammond, E. M., Higgins, G. S., and Petersson, K. (2020a). Corrigendum: Ultra-High
- 997 Dose Rate (FLASH) Radiotherapy: Silver Bullet or Fool’s Gold? *Frontiers in Oncology* 10, 210.
- 998 doi:10.3389/fonc.2020.00210
- 999 Wilson, J. D., Hammond, E. M., Higgins, G. S., and Petersson, K. (2020b). Ultra-high dose rate (flash)
- 1000 radiotherapy: Silver bullet or fool’s gold? *Frontiers in Oncology* 9, 1563. doi:10.3389/fonc.2019.01563
- 1001 Yogo, A., Maeda, T., Hori, T., Sakaki, H., Ogura, K., Nishiuchi, M., et al. (2011). Measurement of relative
- 1002 biological effectiveness of protons in human cancer cells using a laser-driven quasimonoenergetic proton
- 1003 beamline. *Applied Physics Letters* 98, 053701. doi:10.1063/1.3551623
- 1004 Yonemura, Y., Arima, H., Ikeda, N., Ishibashi, K., Maehata, K., Noro, T., et al. (2008). Status of center
- 1005 for accelerator and beam applied science of kyushu university. *EPAC 2008 - Contributions to the*
- 1006 *Proceedings*
- 1007 Zeil, K., Baumann, M., Beyreuther, E., Burris-Mog, T., Cowan, T. E., Enghardt, W., et al. (2013).
- 1008 Dose-controlled irradiation of cancer cells with laser-accelerated proton pulses. *Applied Physics B* 110,
- 1009 437–444. doi:10.1007/s00340-012-5275-3
- 1010 Zlobinskaya, O., Siebenwirth, C., Greubel, C., Hable, V., Hertenberger, R., Humble, N., et al. (2014).
- 1011 The effects of ultra-high dose rate proton irradiation on growth delay in the treatment of human tumor
- 1012 xenografts in nude mice. *Radiation Research* 181, 177–183. doi:10.1667/RR13464.1